This is a preprint, the final version is subject to change, of the American Mineralogist (MSA)
Cite as Authors (Year) Title. American Mineralogist, in press.
DOI: https://doi.org/10.2138/am-2020-7237

REVISION 1

Title: Heavy halogen geochemistry of martian shergottite meteorites and implications for the halogen composition of the depleted shergottite mantle source

Authors: Patricia L. Clay[1*], Katherine H. Joy[1], Brian O'Driscoll[1], Henner Busemann[2], Lorraine Ruzié-Hamilton[1], Ray Burgess[1], Jonathan Fellowes[1], Bastian Joachim-Mrosko[3], John Pernet-Fisher[1], Stanislav Strekopytov[4**] and Christopher J. Ballentine[5]

*corresponding author: (patricia.clay@manchester.ac.uk)

Affiliations: [1]Department of Earth and Environmental Sciences, University of Manchester, Manchester, M13 9PL United Kingdom; [2]Institute for Geochemistry and Petrology, ETH Zürich, Clausiusstrasse 25, 8092 Zürich, Switzerland; [3]Institute for Mineralogy and Petrography, University of Innsbruck, Innrain 52f, A-6020 Innsbruck, Austria; [4]Imaging and Analysis Centre, Natural History Museum, Cromwell Road, London, SW7 5BD United Kingdom; [5]Department of Earth Sciences, University of Oxford, South Parks Road, Oxford, OX1 3AN United Kingdom

**Current address: Inorganic Analysis, LGC Ltd, Queens Road, Teddington TW11 0LY United Kingdom

Manuscript Information: Prepared for submission to American Mineralogist, "Halogens in Planetary Systems" Special Collection. Abstract: 366 words; Main text: 9828 words; References: 108; Figures: 9, Tables: 3; Supplementary Figures: 5; Supplementary Tables: 4

Abstract

Volatile elements (e.g., H, C, N) have a strong influence on the physical and chemical evolution of planets and are essential for the development of habitable conditions. Measurement of the volatile and incompatible heavy halogens, Cl, Br and I, can provide insight into volatile distribution and transport processes, due to their hydrophilic nature. However, information on the bulk halogen composition of martian meteorites is limited, particularly for Br and I, largely due to the difficulty in measuring ppb-level Br and I abundances in small samples. In this study, we address this challenge by using the neutron irradiation noble gas mass spectrometry (NI-NGMS) method to measure the heavy halogen composition of five olivine-phyric shergottite meteorites, including the enriched (Larkman Nunatak LAR 06319 and LAR 12011) and depleted (LAR 12095, LAR 12240, and Tissint) compositional end members. Distinct differences in the absolute abundances and halogen ratios exist between enriched (74 to136 ppm Cl, 1303 to 3061 ppb Br and 4 to1423 ppb I) and depleted (10 to 26 ppm Cl, 46 to 136 ppb Br and 3 to 329 ppb I) samples. All halogen measurements are within the ranges previously reported for shergottite, nakhlite, and chassignite (SNC) meteorites. Enriched shergottites show variable and generally high Br and I

absolute abundances. Halogen ratios (Br/Cl and I/Cl) are in proportions that exceed those of both carbonaceous chondrites and the martian surface. This may be linked to a volatile-rich martian mantle source, be related to shock processes or could represent a degree of heavy halogen contamination (a feature of some Antarctic meteorites, for example). The differences observed in halogen abundances and ratios between enriched and depleted compositions, however, are consistent with previous suggestions of a heterogeneous distribution of volatiles in the martian mantle. Depleted shergottites have lower halogen abundances and Br and Cl in similar proportions to bulk silicate Earth and carbonaceous chondrites. Tissint in particular, as an uncontaminated fall, allows an estimate of the depleted shergottite mantle source composition to be made: 1.2 ppm Cl, 7.0 ppb Br and 0.2 ppb I. The resultant bulk silicate Mars (BSM) estimate (22 ppm Cl, 74 ppb Br and 6 ppb I), including the martian crust and depleted shergottite mantle, is similar to estimates of the bulk silicate Earth (BSE) halogen composition.

Keywords: Mars, shergottites, meteorites, halogens, noble gas, volatile, geochemistry, planetary habitability

Introduction

Volatile elements (e.g., H, C, N) are essential to life on Earth. Dissolved salts, such as chlorides, perchlorates and sulfates, present in aqueous fluids, impact the physical (e.g., freezing point) and chemical (e.g., pH) properties of

these fluids and therefore the ability of surface or subsurface liquid environments to host life. The heavy halogens (Cl, Br and I) are important components of salts in aqueous fluids, such as recently described for subsurface cold brine environments (Stamenković et al. 2018; Orosei et al. 2018) on Mars. Therefore, characterizing the origin and distribution of the halogens in the terrestrial planets is important for a better understanding of planetary habitability potential.

The heavy halogens are highly incompatible and volatile elements, indicating that their general distribution should be influenced by partial melting processes, magmatic fractionation and degassing (Aiuppa et al. 2009). Their hydrophilic behavior means that they are mobilized by, and track with, aqueous fluids. Coupled with their typically low abundances in most geologic materials, these factors make the halogens excellent tracers of volatile evolution and transport processes in terrestrial planets.

Currently, there are three sources of information on the volatile budget of the martian surface and interior: (i) martian meteorites (Cartwright et al. 2013; Filiberto et al. 2016; McCubbin et al. 2016), (ii) orbital measurements (e.g., Mars Odyssey Gamma Ray Spectrometer; Keller et al. 2006) and (iii) *in situ* measurements made by landers (e.g., Viking and Phoenix; Baird et al. 1976) and rovers (e.g., Curiosity, Opportunity and Spirit; Gellert et al. 2004, 2006). Martian meteorites currently offer the only direct source of information on the volatile composition of the martian mantle. The volcanic nature of these samples means they also offer the opportunity to understand volatile transfer processes between the martian mantle and crust. This may provide insight into a planet where plate

tectonic activity, a critical process for volatile transport and recycling through subduction zones on Earth (Holland and Ballentine, 2006), is not thought to have operated. Potential fluid-rock interaction on the surface of Mars may also be recorded in these samples, in the form of alteration products preserved in meteorite samples, though this can be difficult to categorically distinguish from terrestrial alteration of these materials. Bulk rock halogen studies on martian meteorites suggest that Mars is relatively volatile-rich (Dreibus and Wänke, 1985) and *in situ* measurements of Cl and Br on the martian surface suggest a halogen-rich crust (e.g., Gellert et al. 2006), likely due to the presence of alteration mineral-assemblages. However, measurements of OH and halogens in martian apatite and amphibole hosted within volcanic samples are highly variable (Filiberto et al. 2016; McCubbin et al. 2016), indicating that martian mantle volatiles are heterogeneously distributed and that Mars' mantle is similar to, or drier than, currently accepted estimates of terrestrial mantle sources (e.g., Saal et al. 2002).

There are currently only limited bulk heavy halogen measurements available for martian meteorite samples. This is particularly true for Br and I. In this study, we use the NI-NGMS (Neutron Irradiation Noble Gas Mass Spectrometry; Ruzié-Hamilton et al. 2016) method to measure the heavy halogen (Cl, Br and I) abundances and ratios of five shergottite meteorites. Our aim is to characterize the halogen composition of the depleted and enriched shergottite mantle source(s) and thus better constrain the halogen abundance of the martian interior.

By evaluating these measurements in the context of what is known about the abundances of the halogens in the martian crust, we are able to shed light on the halogen budget of the martian mantle. Furthermore, this allows volatile transport mechanisms to be investigated, with broader implications for the role that such fluids play in creating potential habitable environments.

Sample descriptions

Martian meteorites comprise shergottites, nakhlites, and chassingites, collectively known as the SNC's (Bridges and Warren, 2006), as well as the orthopyroxenite Allan Hills (ALHA) 84001 and the grouped 'Black Beauty' breccia samples (e.g., Northwest Africa NWA 7034 and paired stones). Due to the non-cumulate volcanic nature of many of the shergottite meteorites, they can provide constraints on the volatile source composition of the mantle from which they are derived. Shergottites are generally subdivided based on their chondritic-relative rare earth element (REE) geochemistry, into 'enriched' and 'depleted' compositions (Herd et al. 2002; Borg and Draper, 2003). The latter compositional variations have been interpreted to reflect different geochemical reservoirs on Mars (e.g., Symes et al. 2008), or alternatively, varying degrees of crustal contamination and assimilation (e.g., Herd et al. 2002). Recently, enriched and depleted shergottites have been interpreted as representing the products of partial melting of chemically distinct, deep mantle sources (Day et al. 2018) whose reservoirs formed as early as ~4504 Ma (e.g., Borg et al. 2016). Shergottite crystallization ages fall into three distinct groups: ~180 Ma, ~340 Ma

and >474 Ma (Symes et al. 2008; Shafer et al. 2010) with ejection ages that vary from 1.1 ±0.2 Ma (depleted) to ~1-5 Ma (intermediate and enriched) (Lapen et al. 2017). One notable exception is the augite-rich shergottite, NWA 8159, which has a crystallization age of 2.37 ±0.25 Ga (Herd et al. 2017).

The shergottite group contains a range of textural associations, ranging from poikilitic lherzolites (plagioclase-poor), olivine-phyric, and aphyric (commonly referred to as basaltic) (Goodrich, 2002). There is debate over the origin of the olivine-phyric shergottite subgroup, with some favoring an origin by mixing of basaltic and lherzolitic shergottite endmembers (e.g., Mittlefehldt et al. 1999) and others suggesting that the olivine is re-entrained cumulate (e.g., Usui et al. 2008). In this study, five olivine-phyric shergottite meteorites, including the hot desert fall Tissint and four Antarctic find meteorites from the Larkman Nunatak (LAR) icefield (paired stones LAR 06319/12011 and paired stones LAR 12095/12240), are studied. The samples represent both enriched and depleted shergottite compositions. Sample descriptions are summarized below and in Table 1.

Tissint

The Tissint meteorite fell on July 18, 2011 in Morocco (Chennaoui Aoudjehane et al. 2012). As only the fifth observed fall of a martian meteorite, Tissint presents the opportunity to gain insight into the composition of the martian interior and also the products of martian surface alteration, due to short terrestrial residence time and consequent lack of terrestrial alteration (though evidence of

fluid-mineral reaction on Mars' surface is preserved in Tissint; Steele et al. 2018). Tissint is classified as a depleted, olivine-phyric shergottite, based on its bulk and trace element composition (Irving et al. 2012; Chennaoui Aoudjehane et al. 2012), within the range reported for basaltic shergottites. Groundmass and glass-rich samples of Tissint, however, have shown a LREE-enriched component similar to enriched shergottites (Chennaoui Aoudjehane et al. 2012).

Tissint contains large (≤2 mm) crystals of porphyritic olivine in a fine-grained groundmass of olivine (25-28 vol %), maskelynite (a shock-related, high pressure plagioclase pseudomorph; 20-22 vol %), orthopyroxene and clinopyroxene (50-52% vol %) and minor phases including oxides (1-2 vol %), sulfide and phosphates (Balta et al. 2015b). Oxide phases encompass a full compositional range from chromite to ulvöspinel (Balta et al. 2015b). The main sulfide is pyrrhotite. Phosphates are dominantly merrillite, though rare apatite has been documented (Chennaoui Aoudjehane et al. 2012). A crystallization age of 574 ±20 Ma has been reported for Tissint (Brennecka et al. 2014), with initial $^{87}Sr/^{86}Sr$ and $^{143}Nd/^{144}Nd$ compositions distinct from all other martian meteorites, purportedly as a result of its derivation from an incompatible-element depleted mantle source (Brennecka et al. 2014). An ejection age of 0.7 ±0.3 Ma was determined by Chennaoui Aoudjehane et al. (2012). Tissint has been suggested to have formed from closed-system fractional crystallization, representing a previously unsampled member of the shergottite group (Brennecka et al. 2014; Balta et al. 2015b).

183 The majority of martian meteorites are collected as unobserved finds from
184 either hot desert (e.g., Northwest Africa 'NWA', etc.) or cold desert environments
185 (e.g., Antarctica). These environments may affect the primary halogen signature,
186 either through leaching of halogens during terrestrial weathering (Clay et al.
187 2017) or deposition of halogens, particularly Cl and I, from sea spray and methyl
188 iodide contaminants (Langenauer and Krähenbühl, 1993). Tissint in particular, as
189 an observed shergottite fall, therefore offers an excellent opportunity to
190 investigate the primary halogen budget of the depleted shergottite mantle source.
191
192 **LAR 06319 and LAR 12011**
193 LAR 06139 was recovered from the Larkman Nunataks region of the
194 Transantarctic mountains, East Antarctica, in 2006 (McBride et al. 2007) and
195 LAR 12011 was recovered in 2012 (McBride et al. 2013). LAR 06139, and to a
196 lesser extent LAR 12011, have been described in detail by previous workers
197 (Basu Sarbadhikari et al. 2009, 2011, 2016; Balta et al. 2013, 2015a; Howarth et
198 al. 2016; Peslier et al. 2010). Initial characterization of the stones suggested
199 pairing and this was supported by Balta et al. (2015a) on the basis of identical
200 mineralogical and geochemical characteristics. The samples are olivine-pyhric
201 shergottites that contain macrocrysts of olivine up to 3 mm in size (Shafer et al.
202 2010). The matrix consists of olivine (24.4 vol %), pyroxene (54 vol %) and
203 maskelynite (17.8 vol %) with minor phosphate (2.1 vol %), oxide (1.3 vol %) and
204 sulfide (0.3 vol %) (Basu Sarbadhikari et al. 2009). Melt (glass) pockets and
205 shock veins are also observed. Both olivine and pyroxene are compositionally

206 zoned and contain abundant melt inclusions (Basu Sarbadhikari et al. 2009).
207 Brown olivine in LAR 06319 is suggested to have formed during shock
208 metamorphism under high P-T conditions of 30-55 GPa (Takenouchi et al. 2018).
209 A lack of high-pressure phases is attributed to high post-shock temperatures
210 (Fritz et al. 2005). The oxides include chromite to Ti-chromite, and phosphates
211 are apatite, whitlockite and merrillite. The dominantly OH-rich apatites in LAR
212 06139/12011 contain variable abundances of the halogens (Balta et al. 2013;
213 Bellucci et al. 2017). LAR 06139/12011 have an 'enriched' LREE signature
214 typical of other basaltic shergottites (Basu Sarbadhikari et al. 2009; Brandon et
215 al. 2012), relative to the depleted olivine-phyric lherzolitic shergottites. The range
216 in crystallization ages from Ar-Ar (163 ±13 Ma; Park et al. 2009), Rb-Sr (207 ±14
217 Ma; Shih et al. 2009), Sm-Nd (190 ±29 Ma; Shih et al. 2009; 183 ±12 Ma; Shafer
218 et al. 2010) and Lu-Hf (179 ±29 Ma; Shafer et al., 2010) dating for LAR 06139
219 are generally in good agreement. LAR 06139 (and therefore LAR 12011) is
220 interpreted to be the product of partial melting of an incompatible element-
221 enriched, oxidized martian mantle (Basu Sarbadhikari et al. 2009).
222
223 **LAR 12095 and LAR 12240**
224 LAR 12095 and LAR 12240 were recovered from the Larkman Nunataks
225 region of the Transantarctic mountains, East Antarctica in 2012 (McBride et al.
226 2013). They have been described in detail by several previous workers (Howarth
227 et al. 2014; Mikouchi and Takenouchi, 2014; Balta et al. 2015a; Funk, 2015, Funk
228 et al. 2016; Dunham et al. 2019) suggesting that on the basis of petrography,

mineral-chemistry and whole rock major and trace element geochemistry they are paired stones from the same meteorite fall (Dunham et al. 2019). Both are olivine-pyhric shergottites containing olivine phenocrysts up to 3 mm in size, with rare pyroxene macrocrysts up to 2 mm in size. Dunham et al. (2019) characterized the modal mineralogy of LAR 12095/12240 and found the groundmass predominantly comprises olivine (~16-17 vol %), pyroxene (61-62 vol %) and maskelynite (21-23 vol %). Minor phosphates, oxides (~1 vol %) and sulfides (~1 vol %) are also present. Microstructural features of shock metamorphism including abundant melt pockets, veins and darkened olivine are also observed (Dunham et al. 2019). The oxides include chromite and Ti-magnetite, the phosphates are mainly merrillite, with rare apatite, and the sulfide population is dominated by Fe-rich pyrrhotite. LAR 12095/12240 are characterized as depleted shergottites based on their LREE signature (Dunham et al. 2019). There are currently no constraints on the crystallization age of LAR 12240 and LAR 12095, but Righter et al. (2015) suggest an age range of ~400-550 Ma based on the modelled $^{147}Sm/^{144}Nd$ and $^{176}Lu/^{177}Hf$ source composition of depleted shergottite Dar al Gani 476, which represents a close compositional match. Overall, the samples have been interpreted as the products of closed system fractional crystallization, following magma emplacement and crystal accumulation (Dunham et al. 2019).

Methods

Bulk chemical analyses

Bulk chips of LAR 12095/12240 and LAR 06319/12011 were processed for bulk chemical analyses in a class 1000 clean room at the University of Manchester using an agate pestle and mortar. The bulk-rock compositions of LAR 06319,64, LAR 12011,6, LAR 12095,8, and LAR 12240,6 were determined by inductively coupled plasma–mass spectrometry (ICP-MS) using an Agilent 7700x instrument and inductively coupled plasma optical emission spectroscopy (ICP-OES) using a Thermo iCap 6500 Duo spectrometer, at the Natural History Museum, London. The methods used are similar to those reported in Gregory et al. (2017) and are summarized below. Concentrations of 10 major and minor elements including Cr were determined by ICP-OES. The bulk rock major, minor and trace element chemistry of Tissint has been widely reported in the literature (Irving et al. 2012; Chennaoui Aoudjehane et al. 2012; Balta et al. 2015b) and new analyses of this kind are therefore not repeated here.

Approximately 40 mg of sample was fused with 120 mg of $LiBO_2$ in a Pt/Au crucible and the resulting flux dissolved in 10% HNO_3. Calibration was performed using certified reference materials (CRM) prepared in the same way. Concentrations of 38 trace elements as well as K_2O were determined by ICP-MS from a separate portion of ~50 mg of powdered sample after HF + $HClO_4$ + HNO_3 digestion. To minimize polyatomic interferences, the instrument was operated with 5 mL min^{-1} He (99.9995% purity) in the collision–reaction octopole cell (CRC) as well as with no collision gas entering the CRC. Non-isobaric interferences in the ICP-MS analysis were minimized by tuning CeO^+/Ce^+ to

<0.2% (in He mode) and Ba^{++}/Ba^{+} to <1% (both modes). Although most polyatomic interferences are negligible in the He mode, additional mathematical corrections were performed to correct for polyatomic interferences on Eu, Gd, Tb, Hf, Ta, and W caused by Ba, Ce+Pr, Nd, Dy, Ho, and Er, respectively (Strekopytov and Dubinin 1997; Ferrat et al. 2012). Between 3 and 7 repeat measurements of the samples were conducted on different days and the precision of these replicates are reported to 2 standard deviations in Table 2. The relative standard deviation ranges between 0.1% to 5.2% for the major elements, and 0.2% to 7.5% for the minor and trace elements. Accuracy of the ICP-OES analysis was checked by analyzing BHVO-2 Basalt and JG-1 Granodiorite, and of the ICP-MS analysis by analyzing BCR-2 Basalt, SY-2 Syenite, JLs-1 Limestone, and JSd-2 Stream Sediment reference materials (Supplementary Table S1).

Scanning Electron Microscopy (SEM) and Electron Probe Micro-Analysis (EPMA)

Polished thin sections LAR 06319,46, LAR 12011,22, LAR 12095,28, and LAR 12240,17 were optically imaged and then carbon coated for imaging by back-scatter electron imagery using an EDAX EDS system on a Phillips FEI XL30 ESEM-FEG at the University of Manchester.

Electron probe microanalysis on polished sections of all samples was carried out using a Cameca SX100 (LAR samples and Tissint quantitative mineral chemical analyses and qualitative element mapping) and a JEOL JXA-

298 8530F (Tissint qualitative and quantitative element mapping) at the University of
299 Manchester. Olivine, pyroxene, plagioclase, spinel and sulfide compositions were
300 measured in LAR 06319/12011 and LAR 12095/12240. Operating conditions for
301 quantitative analyses in LAR samples using the Cameca SX100 included an
302 acceleration voltage of 15 kV, a beam current of 2 nA (Si, Fe) and 20 nA (Na,
303 Mg, Al, S, Cl, K, Ca, Cr, Mn and Ti) and a spot size of 10 μm. Quantitative
304 analyses of Tissint using the Cameca SX100 used operating conditions including
305 an acceleration voltage of 15 kV, a beam current of 10 nA (Si, Mg, Fe) and 100
306 nA (Al, P, Ca, Ti, Cr, Mn, and Ni) and a spot size of 5 μm. Major and trace
307 element mapping (Mg, Ca, Al, P) was also undertaken to monitor for zoning of
308 particular elements. Analytical conditions for the mapping were variable and are
309 reported in the captions to the Figures and Supplementary Figures.
310

311 **Neutron Irradiation Noble Gas: NI-NGMS and Ar-Ar dating**

312 Bulk heavy halogen (Cl, Br and I) measurements and Ar-Ar dating of
313 Tissint and LAR 06319,64, LAR 12011,6, LAR 12095,8, and LAR 12240,6 were
314 performed at the University of Manchester following the protocols given in Ruzié-
315 Hamilton et al. (2016) and Clay et al. (2017).

316 **Sample preparation and irradiation.** Terrestrial alteration can be
317 problematic for halogen analysis of some meteorite samples and therefore
318 caution was exercised with sample handling, storage and preparation techniques,
319 to avoid the inclusion of weathered material that may be affected by terrestrial
320 alteration. Signs of visible alteration were avoided and material was taken from

the interior portion of the sample to avoid any inclusion of surface material. Prior to irradiation, samples were crushed into small chips and aliquots of ~2-7 mg were extracted. Samples were wrapped in Al-foil and, interspersed with irradiation monitor minerals, encapsulated under vacuum in SiO_2-glass tubing before packing in Al canisters for irradiation. Tissint was irradiated at the SAFARI-1 research reactor, South Africa (irradiation MN17, see Table S3), continuously over a 24-hour period. Larkman Nunatak samples were irradiated at the Oregon State University (OSU) reactor (irradiation MN14a, see Table S3) in a stepped fashion over a 2-month period for a total of ~280 hours. The neutron fluence was monitored in each irradiation with conventional ^{40}Ar-^{39}Ar and I-Xe geochronological standards "Hb3Gr" hornblende (1080.4 ±1.1 Ma; Renne et al. 2010) and enstatite separated from the Shallowater aubrite ($^{129}I/1^{27}I_{initial}$ = 1.072 x 10^{-4}, Brazzle et al. 1999). Scapolite minerals ("BB-1" and "SP"; Ruzié-Hamilton et al. 2016; Kendrick 2012) were used to monitor epithermal neutron fluence. Thermal and epithermal neutron fluxes were ~9.0 x 10^{18} n cm^{-2} and ~1.4 x 10^{17} n cm^{-2} for MN17 and ~6.6 x 10^{18} n cm^{-2} and ~3.4 x 10^{17} n cm^{-2} for MN14a.

NI-NGMS measurements and ^{40}Ar-^{39}Ar dating. Halogen abundances were determined by neutron irradiation noble gas mass spectrometry (NI-NGMS). This method utilizes the neutron-induced conversion of Cl, Br, and I into their respective noble gas isotopes $^{38}Ar_{Cl}$, $^{80,82}Kr_{Br}$ and $^{128}Xe_{I}$. Irradiation of the standards (listed above) with independently known halogen concentrations enables the parent halogen abundances to be accurately calculated from

neutron-produced noble gas isotopes (Böhlke and Irwin 1992; Kendrick 2012; Ruzié-Hamilton et al. 2016).

Samples were analyzed using a Thermo Scientific ARGUS VI^{TM}, a low volume (680 cm^3), Nier-type, static vacuum mass spectrometer designed for multi-collection of Ar isotopes using five Faraday cups and a low mass compact discrete dynode (CDD) ion counting multiplier. Gases were released from meteorite samples using a 55 W Teledyne-CETAC Fusions CO_2 laser with a 3 mm beam diameter. Samples were incrementally step-heated (Ar-Ar) over ~0.2-15 W or fused (halogens) to ~15 W. After release, gases were purified using SAES NP10 getters and then transferred onto a liquid N_2-cooled charcoal finger for five minutes. The finger was warmed to ~60°C to release the gases. A trap current of 230 μA and an acceleration voltage of 2.5 kV were used. We report typical sensitivities of: 1.2 x 10^{-12} cm^3 fA^{-1} Ar, 6.5 x 10^{-13} cm3 fA^{-1} Kr, and 8.3 x 10^{-13} cm^3 fA^{-1} Xe. After nine measurement cycles, isotope abundances were determined by regression to inlet time.

All isotopes were corrected for extraction line blanks, which contributed up to 5%, but typically <1% of ^{38}Ar and <<1% for $^{80,82}Kr$ and ^{128}Xe. All Ar measurements, for both halogen and Ar-Ar age determinations, were corrected for mass discrimination, the radioactive decay of $^{37}Ar_{Ca}$ and $^{39}Ar_K$ between irradiation and analysis time, and for neutron-produced interference reactions. Corrections for air, trapped or cosmogenic contributions based on ^{36}Ar were evaluated on a sample-by-sample basis. Corrections for cosmogenic ^{38}Ar for Tissint were ~ 1-3% and ranged from 2-22% for LAR samples (2-4% in LAR

06319/12011 compared to 15-22% in LAR 12240/12095). Corrections for terrestrial air contamination were negligible. Krypton and Xe isotopes were corrected for neutron-induced fission of ^{235}U using ^{134}Xe. Krypton and Xe were corrected for epithermal neutron production using the scapolite monitor minerals BB1 and BB2/SP and the Shallowater aubrite. All relevant irradiation parameters and correction factors are given in the Supplementary Table S3. The external errors (2σ) are 4% for Cl, 7% for Br and 5% for I, based on the BB1 scapolite monitor.

Natural noble gas measurements

The natural noble gas composition (He, Ne, Ar, Kr and Xe) of aliquots (see Table S4 for masses) of LAR 06319,64, LAR 12011,6, LAR 12095,8, and LAR 12240,6 were determined using the custom-built 'Albatros' mass spectrometer at ETH Zürich. The isotope compositions and concentrations of all noble gases were measured in standard examinations in a single step at ~1700 °C (for further details see Riebe et al. 2017). Typical blanks are (in 10^{-11} cm^3 STP): 0.003, 50, 2, 6, 1900, 0.23 and 0.03 for ^{3}He, ^{4}He (increased due to a short exposure of the gas to a pressure gauge mounted in glass), ^{20}Ne, ^{36}Ar, ^{40}Ar, ^{84}Kr and ^{132}Xe, respectively. Blank contributions to the total released gas are <0.04 % for ^{3}He, ^{21}Ne, 2-12 % for ^{4}He, ^{20}Ne, <2% for ^{22}Ne, ~17/44 % for ^{36}Ar (enriched/depleted), ~4/15% for ^{38}Ar, ~7/23 % for ^{40}Ar, 14-37 % for Kr and 6-40 % for Xe, respectively. The samples were fully degassed in the main temperature steps, as shown with re-extraction steps at slightly elevated temperature. The natural noble

389 gas isotope composition of Tissint is reported by Wieler et al. (2016) and Avice et
390 al. (2018) and is therefore not repeated here.

391 ## Results

392 ### Bulk chemistry

393 Optical and backscattered electron images (BSE) of LAR 12011, 12095
394 and 12240 are provided in Supplementary Figures S1-S3 for reference. Major
395 and trace element sample compositions are reported in Table 2 and plotted in
396 Figure 2 as chondrite-normalized values. Standard data are given in the
397 Supplementary Table S1. There is very good agreement between the enriched
398 LAR 06319/12011 samples. Depleted samples LAR 12095/12240 show slight
399 variation between the two samples (Figure 2). Our bulk analyses of LAR 06319
400 are in broad agreement with previously reported major element measurements
401 (Basu Sarabadhikari et al. 2009); within ~3-5 % for most elements, but up to 8%
402 for Al_2O_3. Our analysis of LAR 12095 agrees with data reported in Funk (2016) to
403 within 2-8% for major elements.

404 ### Element mapping

405 Major (Mg, Ca and Al) and minor element (P) maps of Tissint are shown
406 in Figure 1. Minor element distribution, such as P, can provide insight into the
407 magmatic growth history and cooling history of olivine-bearing rocks (Milman-
408 Barris et al. 2008; Welsch et al. 2014; Watson et al. 2015). The olivine
409 macrocrysts in Tissint show gradational concentric zoning in Mg content of olivine
410 from core to rim, with the highest concentrations in the phenocryst centres (Fig.
411 1a). Distinctive P zoning is observed in Tissint olivine crystals with well-defined

412 dendritic crystallites in macrocryst cores overgown by fine-scale oscillatory
413 zoning (Fig. 1d). Chromium distribution in Tissint matches the same
414 compositional zones as P (Fig. S4). Olivine in the LAR samples was not mapped
415 in the present study but Dunham et al. (2019) reported classic P zoning (P-rich
416 core with alternating low- and high-P zones) in olivine from LAR 12095, and
417 poorly developed zoning in LAR 12240. Balta et al. (2013) additionally reported
418 P-zoning in LAR 06139 olivine.

419 **Mineral chemistry**

420 All of the mineral chemical data are reported in the Supplementary Table
421 S2 and plotted in Figure 3. Balta et al. (2015b) and Dunham et al. (2019)
422 previously reported silicate mineral compositions for samples LAR 12011, 12095
423 and 12240 which are plotted in Figure 3. Mineral compositions for LAR 06319,
424 detailed by Basu Sarabadhikari et al. (2009), Peslier et al. (2010) and Balta et al.
425 (2013) are also plotted for reference in Figure 3. Minor phases, including oxides
426 (spinel and ilmenite) and sulfide (pyrrhotite), were measured in LAR 12240
427 (n=19), LAR 12095 (n=25), LAR 12011 (n=11) and LAR 06139 (n=6) and are
428 reported in Supplementary Table S2.

429 **Maskelynite.** Plagioclase has been converted to maskelynite due to shock
430 metamorphism, as has been observed in martian meteorite samples by other
431 workers (Basu Sarabadhikari et al. 2009; Balta et al. 2013; Dunham et al. 2019).
432 Maskelynite compositions were measured in LAR 12240 (n=65), LAR 12095
433 (n=41), LAR 12011 (n=49) and LAR 06139 (n=9) (Fig. 3a). Maskelynite are low-
434 K, with overlapping compositions in both LAR 12240 and LAR 12095 ranging

435 from $An_{53-71}Ab_{28-46}Or_{0.4-1.0}$, in agreement with the range reported by Peslier et al.
436 (2010) and Dunham et al. (2019). LAR 12011/06139 plagioclase is also
437 converted to maskelynite, albeit relatively K-rich compared to the former
438 samples, with up to $Or_{10.}$ The full compositional range observed is An_{46-59} Ab_{38-}
439 $_{50}Or_{2-10.}$ The latter is a more restricted range for anorthite content in LAR 06139
440 than previous studies (Basu Sarbadhikari et al. 2009; Balta et al. 2013), with
441 similarly high K-contents as reported in Balta et al. (2013).

442 **Pyroxene.** Pyroxene compositions were measured in LAR 12240 (n=113),
443 LAR 12095 (n=77), LAR 12011 (n=105) and LAR 06139 (n=33) (Fig. 3b) and
444 show a wide range of compositions. Pyroxene compositions in LAR 12240/12095
445 overlap, similar to the data of Dunham et al. (2019). The measured compositions
446 are dominated by low Ca-pigeonite with a small number of augite analyses. The
447 full range of compositions is $En_{44-72}Fs_{18-35}$ Wo_{4-37} and Mg# 62-76. LAR
448 12011/LAR 06319 also overlap in composition, with a range of $En_{38-71}Fs_{17-47}Wo_{4-}$
449 $_{36}$ and Mg# 46-73, and show more variation in their Fe-contents compared with
450 the LAR 12240/12095 pair. Low-Ca pigeonite also dominates, with minor augite
451 present too. A subset of typically more Fe-rich pyroxene measurements from
452 LAR 12011 (n=17), in contact with a pseudomorphed glass pocket, show a large
453 range of compositions of $En_{39-69}Fs_{23-45}Wo_{4-30}$ and Mg# 46-72. Pyroxene crystals
454 in Tissint (n=6) yield compositions of $En_{51-64}Fs_{25-27}Wo_{8-24}$ and Mg# 67-70.

455 **Olivine.** Olivine compositions were measured in LAR 12240 (n=42), LAR
456 12095 (n=30), LAR 12011 (n=61) and LAR 06139 (n=77) (Fig. 3c and 3d).
457 Olivine compositional ranges between LAR 12240 and 12095 show good

458 overlap, as observed by Dunham et al., (2019). We report a range in
459 compositions of $Fo_{57-66}Fa_{34-43}$ and FeO/MnO=51-59. Olivine cores are typically
460 more Mg-rich than the rims. LAR 12011 and LAR 06319 overlap in composition,
461 but yield more variable olivine compositions, with a full range of $Fo_{48-79}Fa_{21-52}$ and
462 FeO/MnO=46-57. Olivine was measured in Tissint (n=66) and revealed a range
463 of $Fo_{52-79}Fa_{21-47}$ and FeO/MnO of 36-47.

464 **Halogen geochemistry**

465 Results from all heating experiments are reported in Table 3 and Figures 4
466 and 5. Chlorine in Tissint (n=6) ranges from 15.9 ±3.4 to 26.0 ±5.5 ppm. Bromine
467 and I (n=4) range from 103 ±22 to 136 ±29 and 3.4 ±0.7 to 5.7 ±1.1 ppb,
468 respectively (Fig. 4a and 4b). Average concentrations (1σ S.D) of 21.2 ±3.8 ppm
469 Cl, 120.8 ±14.3 ppb Br and 4.1 ±1.1 ppb I in Tissint (Table 3) are within the range
470 of previously measured halogen concentrations in SNCs (see Rampe et al. 2018
471 and values and ranges given in Fig. 4 and Table 3), though on the lower side of
472 previously reported abundances.

473 Depleted shergottites LAR 12240/12095 yield Cl abundances of 10.1 ±0.5
474 to 15.8 ±0.8 ppm, 46 ±3 to 62 ±4 ppb Br and a variable distribution of I of 59 ±4 to
475 78 ±5 for LAR 12095 and 259 ±17 to 329 ±22 for LAR 12240 (Fig. 4a and 4b).
476 The enriched shergottites LAR 12011/06139 yield Cl abundances of 73.5 ±3.5 to
477 136.1 ±6.4 ppm and have heterogeneous Br (1213 ±94 to 3061 ±215 ppb) and I
478 (4 ±1 to 1423 ±95 ppb) abundances (Figs. 4a and b). The depleted shergottites
479 (LAR 12240/12095) yield more consistent results compared to the enriched pair
480 (LAR 12011/06319) but all abundances are within the range of what has been

481 measured previously for bulk rock halogens in SNC meteorites (data ranges and
482 references are given in Table 3 and plotted for comparison in Figure 4).

483 Potassium, Ca and Ba concentrations are derived from the measurement
484 of ^{39}Ar, ^{37}Ar and ^{130}Xe, respectively. Potassium concentrations in Tissint (n=6)
485 range from 229 ±41 to 291 ±52 (average of 265 ±25 1σ SD, n=6). Barium
486 concentrations range from 1.3 ±0.3 to 1.9 ±0.4 (average of 1.7 ±0.3 1σ SD, n=4),
487 lower than the Ba concentration of 5.9 ppm reported by Avice et al. (2018).
488 Potassium from two measurements of LAR 12240 (174 ±6 and 133 ±4 ppm) and
489 LAR 12095 (149 ±5 and 145 ±5 ppm) generally agree with the values determined
490 by ICP-MS (Table 1). Barium from LAR 12240 (2.0 ±0.2 to 1.5 ±0.1 ppm) and
491 LAR 12095 (1.8 ±0.2 to 1.9 ±0.2 ppm) also agree with the Ba abundances
492 determined by ICP-MS. Calcium abundances are not reported due to the
493 timescale between irradiation and analysis (>5 months, $t_{1/2}$ $^{37}Ar_{Ca}$ ~35.1 days)
494 and the consequent higher uncertainty associated with these measurements
495 compared to other reported bulk Ca determinations.

496 Tissint yields Br/Cl and I/Cl ratios of 4.9 ±0.2 to 7.3 ±0.3 ($\times10^{-3}$) and 0.13
497 ±0.04 to 0.29 ±0.08 ($\times10^{-3}$). The highest I/Cl ratios for Tissint result from slightly
498 lower Cl abundances (~16-20 ppm Cl in two of the measured samples (H-1 and
499 H2; Fig. 5, Table 3). The K/Cl ratio of Tissint is reproducible, ranging from 11.2
500 ±2.0 to 14.4 ±2.6 (Fig. 4c).

501 Depleted shergottites LAR 12240/12095 yield similar Br/Cl ratios of 3.9
502 ±0.3 to 4.5 ±0.4 ($\times10^{-3}$). The I/Cl ratios vary by sample, mostly due to the variable
503 I abundances between the pairs: 20.8 ±1.7 and 25.6 ±2.1 ($\times10^{-3}$) for LAR 12240

and 3.9 ±0.3 and 6.1 ±0.5 ($\times 10^{-3}$) for LAR 12095. Paired, enriched shergottites LAR 12011 and 06139 yield Br/Cl ratios of 3.9 ±0.3 to 4.5 ±0.4 ($\times 10^{-3}$). The I/Cl ratios are relatively heterogeneous and range from 0.03 ±0.01 to 2.1 ±0.2 ($\times 10^{-3}$), due to the three orders of magnitude variation in the measured I abundances between the two samples (Fig. 5). The K/Cl ratio of all, both depleted and enriched LAR samples, is broadly similar and ranges from 11.0 ±0.4 to 13.3 ±0.4, with the exception of one lower reported value of 9.6 ±0.3 (LAR 12095 split I, Table 3). These ratios are also broadly consistent with Tissint and previous measurements for the K/Cl ratio in shergottites (K/Cl ~15; Wänke and Dreibus, 1994).

^{40}Ar-^{39}Ar dating

All ^{40}Ar-^{39}Ar data, including irradiation parameters and all correction factors, are reported in Supplementary Table S3 and Figure S5. After correction for cosmogenic and atmospheric components (Wiens et al. 1986, Wieler, 2002, Avice et al. 2018) were accounted for (see Table S3), age spectra for each sample were plotted. No plateau ages (where plateau steps are defined as contiguous steps comprising >55% of the total ^{39}Ar released and overlapping within uncertainty) were determined for any of the samples, indicating disturbed Ar systematics for these shergottite samples. Two splits of the Tissint meteorite (Tissint D1, 6.7 mg and Tissint D-2, 7.1 mg, Fig. S5a and 5b) yielded age ranges of 502 to 1072 Ma and 664 to 2178 Ma over 20 heating steps and 12 heating steps, respectively. Tissint (D-1) gives four high-T steps that are consistent with

the crystallization age of Tissint (574 ±20 Ma; Brennecka et al. 2014) ranging from 549 ±3 to 576 ±2 Ma, but comprising <35% of the total ^{39}Ar.

Splits of paired samples LAR 06319 (2.36 mg, n=17 steps Fig. S5c) and LAR 12011 (1.99 mg, n=16 steps, Fig. S5d) gave age ranges of 247-389 Ma and 156 to 342 Ma, respectively. No plateau ages were determined for these samples which yielded different isochron ages and trapped ^{40}Ar/^{36}Ar compositions. LAR 06319 yielded an isochron age of 301 ±30 Ma while LAR 12011 yielded an isochron age of 127 ±25 Ma. The LAR 12011 age is just within uncertainty of an Ar-Ar age of 163 ±13 Ma determined in pair LAR 06319 (Park et al. 2009). LAR 06319, however, exceeds this age as well as age determinations from other isotopic systems, including Rb-Sr (207 ±14 Ma; Shih et al. 2009), Sm-Nd (190 ±29 Ma; Shih et al. 2009; 183 ±12 Ma; Shafer et al. 2010) and Lu-Hf (179 ±29 Ma), suggesting complex Ar-Ar histories in these paired samples which may be due to shock processes that can disturb Ar distribution.

One split of LAR 12240 (2.01 mg, n=14 steps) was measured and yielded age ranges of 571 to 1550 Ma. Whilst no plateau age was determined for this sample, a weighted mean average of 4 high-temperature steps comprising 35% of the ^{39}Ar yields an age of 581 ±2 Ma which is slightly higher than the isochron age of 501 ±35 Ma, Fig. S5e). No crystallization age has previously been determined for comparison with paired samples LAR 12240/12095; however, these ages are broadly similar with a previous model estimate of ~400-500 Ma (Righter et al. 2015).

Natural noble gas composition

Natural noble gas data are reported Supplementary Table S4. As is typical for shergottites (e.g. Cartwright et al. 2014; Wieler et al. 2016), the light noble gases contain mostly only cosmogenic (cos) He and Ne and radiogenic (rad) ^{4}He (Table S4a). The measured ^{3}He is entirely cosmogenic, and can be used directly for cosmic ray exposure (CRE) age determinations. Using $(^4He/^3He)_{cos}$ = 5.65 ±0.45 to correct for $^4He_{cos}$ we obtain $^4He_{rad.}$ This is very low in all samples and quite constant in the two depleted LAR samples (12095/12240) but variable in the two enriched LAR samples (06319/12011).

The Ne isotopic compositions of the four LAR samples and Tissint (Wieler et al. 2016) are shown in Figure 6. The two enriched LAR samples contain a small trapped Ne component. It is not possible to distinguish whether it is Martian or terrestrial, due the proximity of the data points to the cosmogenic Ne region. For decomposition, we used air Ne. The depleted LAR samples do not show any trapped Ne, however, a contribution from SCR Ne, which is typical for small shergottites (Wieler et al. 2016), is revealed. The measured $^{36}Ar/^{38}Ar$ ratios were used to determine $^{38}Ar_{cos}$ assuming air Ar as trapped and a ratio of 0.65 ±0.02 as a cosmogenic endmember composition. We used the model predictions by Leya and Masarik (2009, and updates, pers. comm.) based on a physical model for ordinary chondrites, shielding constraints parameterized by the “shielding parameter” $(^{22}Ne/^{21}Ne)_{cos}$ or its inverse, and bulk chemistry of the main target elements for the production of cosmogenic ^{3}He, ^{21}Ne and ^{38}Ar (Table 2). For the enriched LAR samples, we adopted $(^{21}Ne/^{22}Ne)_{cos}$ in the range 0.80 to 0.85 (by

573 extrapolation into the cosmogenic Ne region, Fig. 6). For the depleted LAR
574 samples, the measured Ne was used which is affected by SCR-Ne contributions.
575 All $(^{21}Ne/^{22}Ne)_{cos}$ ratios are at the low range expected for GCR-Ne, suggesting,
576 as for many other shergottites (Wieler et al. 2016), a small pre-atmospheric entry
577 size or/and contributions from SCR-Ne. Following Wieler et al. (2016, their Fig.
578 3), we tested the presence of SCR-Ne. The elemental ratio Mg/(Al+Si) for LAR
579 06319 and 12011 are 0.40 and 0.38, respectively. Combined with the deduced
580 $(^{21}Ne/^{22}Ne)_{cos}$, the presence of SCR-Ne is possible but not proven or necessary
581 to explain the data for these meteorites. We assume GCR production only. The
582 opposite, however, is true for the depleted samples LAR 12240 and 12095. Both
583 samples have seen SCR and must originate from the surface of the meteoroid.
584 The CRE ages determined on GCR-Ne systematics alone will hence be
585 underestimated.

586 The model calculations allow various shielding conditions, but (after
587 excluding extreme and unrealistic radii of ≥120 cm) all conditions include only
588 surface locations for the samples in the meteoroid and essentially all pre-
589 atmospheric radii. For the production rates we somewhat arbitrarily allow pre-
590 atmospheric radii of at max. 20 cm (which would be a sphere of 108 kg assuming
591 a density of 3.22 g/cm^3). This means for all samples already that the found
592 masses represent only ≤0.7 % (LAR 12201) or ≤0.12 % (the other samples) of
593 the meteoroid and our assumption is thus very conservative. The uncertainties of
594 the resulting production rates for ^{3}He, ^{21}Ne and ^{38}Ar include these allowed
595 shielding conditions (Table S4e). For LAR 12095 and 12240, the model (Leya

596 and Masarik, 2009, including update for meteoroids with ≤7 cm radii) predicts no
597 $(^{21}Ne/^{22}Ne)_{cos}$ ratios similar to the measured ratios due to SCR. We use the
598 chemistry-dependent production rates determined for 10 and 20 cm radii and
599 shielding depth of 0-3 cm as a rough estimate (Table S4e).

600 The radiogenic ^{4}He and ^{40}Ar can also be used to determine, albeit only
601 rough maxima, K-Ar and U/Th-^{4}He ages using the chemistry in Table 2 and gas
602 concentrations in Table S4. Maximum K-Ar and U/Th-^{4}He ages for the enriched
603 LAR 12011/06319 are ~0.4/0.5 Ga and 2/11 Ma, for the depleted LAR
604 12240/12095, ~1.1/1.3 Ga and 66/84 Ma, respectively.

605 Within their large uncertainties the Kr and Xe isotopic compositions of all
606 LAR samples are broadly consistent with a mixture of trapped and cosmogenic
607 Kr and Xe. The uncertainties are too large to decide whether the trapped
608 component is air or martian but most data points are more consistent with air.
609 There is no evidence for neutron-derived excesses in $^{80,82}Kr$ and ^{128}Xe, in
610 agreement with the assumed small sizes of the meteoroids (see above), the
611 origin of the samples from the meteoroids' surface and small abundances of Br
612 and I. LAR 12011 shows the least Xe air contamination and, hence the highest
613 $^{129}Xe/^{132}Xe$ ratio and the highest portion of cosmogenic Xe. In an $^{129}Xe/^{132}Xe$ vs.
614 $^{36}Ar_{tr}/^{132}Xe$ plot (not shown, cf. Fig. 3B in Cartwright et al. 2014), only LAR 12011
615 plots on the mixing line between Mars' interior and atmosphere, typical for
616 uncontaminated shergottites whereas the other three LAR samples plot close to
617 "Earth fractionated atmosphere", which illustrates that the small trapped Kr and
618 Xe amounts in these samples are likely air.

Thus, the two pairs of enriched and depleted LAR samples were ejected from Mars at different times. Depleted shergottite Tissint (CRE age 0.7 ±0.3 Ma, Chennaoui Aoudjehane et al. 2012) and the depleted LAR 12240/12095 (lower limit, see above, 0.84 ±0.15 Ma, Table S4e) could have been ejected in the same event, whereas LAR 06319/12011 were ejected from Mars later, at 0.35 ±0.05 Ma ago.

Data quality and evaluation of potential halogen sources

The present study documents distinct bulk rock halogen geochemical characteristics between depleted and enriched shergottite meteorites. Both sets of samples reveal halogen abundances and ratios consistent within what has been previously reported for other shergottite meteorites (e.g., Rampe et al. 2018 and references therein). However, the differences between the enriched and depleted endmembers are significant: the depleted shergottites, particularly Tissint, have low halogen abundances that are generally consistent with each other, whereas the enriched shergottites have variable and high Br concentrations and generally higher and also relatively variable I abundances (~4× orders of magnitude). Robust characterization of bulk martian meteorites is a particular challenge for trace and mobile elements like the halogens because most martian meteorites are finds and have variable and sometimes long terrestrial residence times prior to collection, often in hot or cold desert environments. Additionally, the typically small sample masses available for study complicates our ability to robustly characterize the ppb to ppm level halogen abundances normally present in these samples. It is therefore particularly

642 important to consider all potential sources of the halogens before attempting to
643 link the measurements to a particular source region or geochemical process.
644 Here, we consider several potential halogen sources and processes, including:
645 terrestrial contamination (i.e., Langenauer and Krähenbühl, 1993), martian
646 surface alteration including secondary mineral assemblages (i.e., Bridges et al.
647 2001), shock metamorphism (Nyquist et al. 2001), the role of primary mineral
648 carrier phases, such as apatite (Howarth et al. 2016; McCubbin et al. 2016) and
649 crustal contamination processes.

650 **Terrestrial alteration.** Terrestrial halogen contamination and alteration of
651 meteorites with a prolonged residence at Earth's surface have been documented
652 in both cold desert (Langenauer and Krähenbühl, 1993) and hot desert (Clay et
653 al. 2017) environments and can be characterized by either halogen deposition
654 (e.g., I, cold desert) or leaching (e.g., Br, hot desert). The effects of terrestrial
655 contamination can largely be mitigated through sample preparation techniques
656 that avoid inclusion of surface material. Whilst we do not document any
657 secondary alteration assemblages of features such as Ca-veining, previous
658 studies (e.g., Dunham et al. 2019) report elevated S concentrations in cracks and
659 sulfate phases intergrown with phosphates that are likely the result of such
660 alteration processes. Funk (2016) reported more extensive alteration in LAR
661 12095 compared to LAR 12240 based on elevated S concentrations. In the case
662 of Tissint, contributions from terrestrial alteration can effectively be ruled out due
663 to the short (months) time between fall and collection. This is evidenced by low

664 and reproducible halogen abundances (Fig. 4, Table 3) between multiple sample
665 splits.

666 Terrestrial alteration may be suspected by high halogen abundances (e.g.,
667 LAR 06319 split I, ~1400 ppb I) but the K/Cl and Cl/La ratios can also be used to
668 discriminate alteration processes (Filliberto et al. 2016). The K/Cl ratio of all
669 shergottite samples in this study range from 9.6 ±0.3 to 14.4 ±2.6,
670 indistinguishable from the K/Cl ratio of previously reported shergottite meteorites
671 (K/Cl ~15; Wänke and Dreibus, 1994). The Cl/La ratios of the enriched
672 shergottites (Cl/La = 43 and 67; Fig. 7a and 7b), the most likely to be affected by
673 terrestrial alteration based on their high Br and I concentrations, are generally
674 consistent with the ratio for the martian interior (Cl/La ~52; Filliberto et al. 2016).
675 Barium measured by NI-NGMS is consistent within samples and comparable to
676 previous work (e.g., Balta et al. 2015).

677 With the exception of the heavy noble gases Kr and Xe, LAR 12240 and
678 LAR 12095 do not seem to be affected by terrestrial alteration based on
679 petrography, geochemistry and generally low and constant halogen abundances
680 (Figure 5). The high Br abundances in LAR 06319 and LAR 12011, as well as
681 one high I measurement in LAR 06319, warrant further consideration, particularly
682 as these are Antarctic meteorites. However, the petrography and other
683 geochemical evidence (e.g., K/Cl, Cl/La, Ba) suggest that alteration is unlikely
684 unless it affected exclusively Br (and I in one sample), but did not modify Cl and
685 other mobile elements like Ba and K.

686 **Secondary alteration assemblages.** There is abundant evidence in the
687 SNC meteorite collection for the presence of secondary mineral assemblages
688 (Bridges et al. 2001). These minor phases (≤1 vol %), in the form of sulfate,
689 carbonate, halite and clay minerals, provide a record of fluid-rock and surface
690 reservoir interaction on the martian surface. Unlike terrestrial alteration, which
691 can typically be avoided through sample preparation techniques, martian
692 secondary alteration phases cannot easily be avoided in bulk analyses, are a
693 potential host of halogens (e.g., halite), and can obscure primary magmatic
694 signature(s). Shergottites are not known to contain secondary mineral
695 assemblages (Hallis et al. 2017), based on overall lower water contents,
696 compared to the nakhlites and the orthopyroxenite ALHA 84001 (Karlsson et al.
697 1992; Bridges et al. 2001), though Steele et al. (2018) describe likely mineral-
698 fluid reactions in Tissint. The martian surface is comprised of dust, rocks and soil
699 of a basaltic composition similar to shergottites and rich in salts (Gellert et al.
700 2004). The relationship between the surface composition of Mars and the
701 observed alteration assemblages in SNC meteorites is unclear; however, the role
702 of brines and evaporative processes has been suggested to be important in the
703 formation of these assemblages (Rao et al. 2005). The heavy halogen
704 composition of these alteration assemblages is not currently well constrained,
705 particularly for I. However, Cl and Br data from nakhlite alteration veins (7700
706 ppm Cl, 151 ppm Br, Br/Cl (w/w) ~ 0.02; Rao et al. 2005) suggest similar
707 compositions to terrestrial brines, in excess of abundances and ratios measured
708 (~350× Cl, ~1100× Br and ~4-5× Br/Cl) in the depleted shergottite samples here.

709 The ratio of Cl/La in enriched shergottites (Cl/La = 43 and 67; Fig. 7) is similar to
710 the ratio for the martian interior (Cl/La ~ 52; Filliberto et al. 2016) and lower than
711 the range for crustal regolith breccias (Cl/La = 97-190; where a high Cl/La ratio is
712 indicative of alteration), which are considered to contain a component of martian
713 surface material.

714 Martian alteration assemblages probably do not contribute to the halogen
715 budget of the depleted shergottite samples, but cannot be definitively ruled out as
716 contributors to the halogen budget of the enriched shergottite samples LAR
717 06319/12011, due to the similarity in the proportion of Br to Cl present in these
718 samples to measured secondary salt vein material in other martian meteorites
719 (Br/Cl ~20 $\times 10^{-3}$). We suggest that it is unlikely however, despite the similarity in
720 Br/Cl ratios, due to a lack of petrographic evidence for alteration assemblages in
721 these samples, coupled with K/Cl and Cl/La ratios that are different to martian
722 surface values.

723 **Iodine and the role of shock.** All martian meteorites show evidence of
724 shock metamorphism, resulting from the large-scale impacts that ejected them
725 from the surface of Mars (Nyquist et al. 2001). Shock implantation of martian
726 atmospheric gases into meteorites (Ocker and Gilmour 2004; Cartwright et al.
727 2010) occurred with shock pressures ranging from 15 to 45 GPa (Fritz et al.
728 2005). This is evidenced particularly in $^{129}Xe/^{132}Xe$ ratios that exceed that of solar
729 (1.0450 ±0.0050; Crowther and Gilmour 2013) or the trapped 'planetary'
730 component Q-Xe (1.042 ±0.002; Busemann et al. 2000) preserved in glass,

731 opaque mineral phases, maskelyinite and pyroxene in martian meteorites (Ocker
732 and Gilmour 2004; Cartwright et al. 2010).

733 Iodine, as a large ion, would be particularly susceptible to mobilization and
734 redistribution due to shock metamorphism. Iodine abundances measured in the
735 samples in this study are variable with the exception of Tissint (4.1 ±1.1 ppb I,
736 1σ, n=4). The enriched shergottite samples range from ~4-200 ppb, with the
737 exception of one of the subsamples of LAR 06319 (split I, ~1400 ppb I), while
738 depleted shergottite samples LAR 12095/12240 range from ~60-330 ppb I. This
739 variation of ~4 orders of magnitude could result from shock processes and a
740 relationship between the $^{129}Xe/^{132}Xe$ ratio and I abundance might therefore be
741 expected. The $^{129}Xe/^{132}Xe$ ratios of depleted shergottites are 0.989 ±0.28 and
742 1.014 ±0.044 and of enriched shergottites are 1.006 ±0.019 and 1.34 ±0.13.
743 Avice et al. (2018) report $^{129}Xe/^{132}Xe$ ratios of 1.147 ±0.348 to 2.030 ±0.012 in
744 bulk samples and glass separates (the highest ratios are preserved in Tissint
745 glass). With only one enriched sample (LAR 12011) and one depleted sample
746 (Tissint) in excess of the solar, air or trapped planetary $^{129}Xe/^{132}Xe$ values, and
747 no correlation with I concentration, the role of shock on the I budget is difficult to
748 assess here. Further halogen and noble gas measurements on variably shocked
749 martian meteorites, including I abundances in specific mineral phases with
750 documented excesses in $^{129}Xe/^{132}Xe$ (Cartwright et al. 2010, 2014), will help
751 elucidate the influence that shock has on I (re)distribution in future studies.

752 **Halogen carrier phases and mineralogical control.** Constraining
753 particular mineralogical control(s) on halogen abundances can be difficult

754 because measuring halogens in major rock-forming, but halogen-poor, silicate
755 minerals, such as olivine and pyroxene, can be challenging. The effect of
756 volumetrically minor but halogen-rich phases, such as apatite, on the bulk
757 halogen signature of meteorites is more straightforward to estimate. Complete Cl,
758 Br and I datasets for apatite are uncommon; however, Bellucci et al. (2017)
759 report apatite compositions from enriched (including LAR 12011) and depleted
760 shergottites that can be used to estimate if apatite might in principle account for
761 the halogen abundances and distributions observed here. Figure 8 shows the
762 relative contributions of varying modal proportions of apatite on bulk rock halogen
763 abundances for “halogen-rich” (enriched shergottite LAR 12011; Bellucci et al.
764 2017) and “halogen-poor” (depleted shergottite SaU 005; Bellucci et al. 2017)
765 apatite compositions. The Br and I composition of Tissint could be accounted for
766 by ~0.1 vol % (I) to 1.7 vol % (Br) apatite, but requires ~ 13.5 vol % for Cl,
767 suggesting a simple apatite control does not adequately explain our data. We
768 note that the halogen composition of merrillite reported by Bellucci et al. (2017)
769 for Tissint is similar to the apatite composition for depleted shergottites and
770 therefore may represent a reasonable halogen carrier. Depleted samples LAR
771 12240/LAR 12095 would require apatite to be present in quantities between ~0.6
772 to 11 vol % of the rock to account for the full range of bulk halogen abundances
773 in these samples. Enriched shergottites LAR 06319/ LAR 12011 would require
774 apatite abundances of 0.1 and 2.1 vol % for Cl and Br, respectively, but up to 40
775 vol % of apatite to account I. Given the significant variation in apatite
776 composition, from halogen-rich chlorapatite to more halogen-poor OH-apatite

(e.g., Bellucci et al. 2017) we suggest that apatite is likely an important halogen carrier phase, though additional carrier phase(s) or secondary process(es) are required to account for the discrepancy in Cl and Br/I concentrations and Br/Cl and I/Cl ratios, between apatite and bulk martian meteorites. Other potential halogen sites within the samples include grain boundary networks and defects or inclusions in olivine or pyroxene, which could account for the variation in ratios between bulk samples and apatite. This is evidenced by the relationship between Cl and P_2O_5. Rather than a positive correlation, which would indicate apatite as the sole carrier for Cl in these samples (Fig. 7c), we observe the depleted shergottites clustering in relatively low bulk Cl versus P_2O_5 space, distinct from the enriched shergottites which have higher coupled P_2O_5 and Cl abundances.

Crustal contamination. The halogen concentrations in the enriched shergottites are relatively high compared with the depleted shergottites, but are also variable. The source of the REE enrichments in these samples is currently an issue of some debate, with suggestions ranging between contributions from an enriched mantle source (Symes et al. 2008) and the role of crustal contamination of shergottite magmas (Herd et al. 2002). On Mars, like Earth, halogens are concentrated in the crust relative to the mantle and, therefore, the effects of crustal contamination of a magma can possibly be discriminated. Previous work on stable isotope variations in martian samples, (e.g., $\delta^{34}S$, Franz et al. 2014; $\delta^{37}Cl$, Williams et al. 2016), supports interaction of magma with the martian crust. However, models of magma-crust mixing and assimilation between depleted shergottite compositions and regolith breccia NWA 7034 (Brandon et al.

2017), the latter as an analog for the ancient martian crust, do not support crustal contamination and suggest that the REE enrichment is a feature of the primary mantle source.

Here, we observe consistently elevated Br (up to ~3000 ppb) and variable, but elevated, I abundances (~4–1423 ppb) in enriched samples (LAR 06319/12011) which could indicate the contamination of a depleted shergottite magma by martian crustal material. The Br/Cl and I/Cl ratios of enriched shergottites are distinct from depleted shergottites and higher than both carbonaceous chondrites and the Br/Cl ratio of the martian surface (Taylor et al. 2010; Figs. 4a and 4b). The K/Cl ratio of enriched shergottites, however, is inconsistent with that of the martian surface (Fig. 4c). Additionally, the Cl/La ratio of enriched shergottites is low and consistent with that of the putative martian interior (Fig. 7; Filiberto et al. 2016). Interaction with the martian surface is not evidenced, as this would require a high Cl/La ratio (Cl/La>100). Crustal contamination is therefore not thought to be important to the halogen signature of the enriched shergottites studied here on the basis of the different K/Cl and Cl/La ratios, but cannot be conclusively ruled out.

Discussion

Halogen geochemistry of the depleted vs enriched shergottites

Depleted shergottites Tissint, LAR 12240 and LAR 12095 yield halogen abundances that range from 10 to 26 ppm Cl, 46 to 136 ppb Br and 3 to 329 ppb I (Fig. 4a and 4b). Enriched shergottites LAR 12011 and LAR 06139 yield Cl

abundances 74 to 136 ppm Cl, 1303 to 3061 ppb Br and ~4 to 1423 ppb I (Fig. 4a and b). In general, depleted shergottites yield more consistent results compared to the enriched shergottites, yet all are within the range of previously reported bulk martian halogens (Figs. 4 and 9) from meteorites. Enriched shergottites are more halogen-rich than depleted shergottites (Figure 9) and show similar CI-chondrite relative enrichment/depletion abundance patterns to other mobile, incompatible lithophile elements (e.g., Ba, Rb; Figs. 2a and 9) suggesting similar behavior. Significant variation in I abundance is seen across both enriched and depleted shergottites and ranges from ~0.1 to 25 × CI chondrite abundance and may reflect the variety of factors that may affect I (as discussed above). Our results suggest the enriched and depleted shergottite mantle sources have distinct halogen geochemical signatures. Moreover, the reproducible halogen abundances in the Tissint meteorite in particular offer an opportunity to better understand the halogen geochemistry of the martian mantle.

Tissint as a proxy for the martian mantle

As an unaltered meteorite fall with reproducible halogen abundances between multiple subsplits, the Tissint meteorite halogen composition can be used to estimate the halogen composition of the depleted shergottite mantle source. Before doing so, it is useful to briefly review what is known about the petrogenesis of the Tissint meteorite for wider context.

Tissint petrogenesis. There has been some discussion in the literature about the origin of the olivine macrocrysts in Tissint, i.e., as either phenocrysts *sensu stricto* (Liu et al. 2016), grown in chemical equilibrium with their host rock,

or as antecrysts (Balta et al. 2015a). The arguments of Liu et al. (2015) are partly based on a lack of evidence of resorption in fine-scale P zoning in olivine. Phosphorous is a particularly useful element to constrain crystallization kinetics in olivine, in which it diffuses relatively slowly (Welsch et al. 2014; Watson et al. 2015). Our P mapping in olivine are somewhat ambiguous, in that one of the crystals in Figure 1d may exhibit resorption surfaces, but the other does not. However, an equally interesting microstructural feature of our P mapping is the excellent preservation of primary dendritic crystallites in the cores of some crystals. The exposure of such dendrites is generally dependent on the 2D intersection of the olivine crystal in question, so they might be much more widespread than presently observed in the Tissint meteorite. The presence of these dendrites, particularly when coupled with the observation that the distribution of Cr (which diffuses an order of magnitude faster than P in olivine) preserves the same structure, has implications for the growth rate and cooling history of the Tissint macrocrysts. In essence, we suggest that it is very unlikely that the olivine crystals in Tissint formed in a cumulate that remained at high temperature for any protracted (several months) period of time (Welsch et al. 2014; Watson et al. 2015). For example, at 850 °C, using the diffusion parameters provided in Watson et al. (2015) for P in olivine, it would take only ~100 days for P to diffusively equilibrate over a length-scale of 5 μm, effectively erasing the evidence of fine-scale P-zoning. Furthermore, the preservation of Cr-zoning in Tissint olivine (Fig. S4), a faster diffuser than P, requires an even faster cooling regime. This suggests that even though localized evidence of resorption

on olivine surfaces may exist, the Tissint olivine macrocrysts are more likely to be phenocrysts rather than a re-entrained cumulate and are in, or close to, chemical equilibrium with their host groundmass. Assuming that the same can be said for the remainder of the crystal cargo in the Tissint meteorite, in particular the dominant halogen carrier phase(s) such as apatite, then the bulk rock (groundmass plus crystals) may be considered as a closed system and thus represent a good proxy for extrapolating backward to its mantle source composition.

Depleted shergottite source composition and bulk silicate Mars. Based on the previous discussion, we use halogen abundances in the Tissint meteorite to estimate the composition of the depleted shergottite mantle source. Furthermore, in conjunction with reported halogen compositions of the martian crust (Gellert et al. 2004, 2006; Keller et al. 2006; Taylor et al. 2010), an estimate of the halogen composition of bulk silicate Mars (BSM) can be calculated. The mass of Mars is 6.2×10^{23} kg, of which the martian crust and mantle are modelled to be ~5.8% and 94.2%, respectively (e.g., Goettel, 1981). Using the average halogen composition of Tissint yields a depleted shergottite source composition of 1.2 ppm Cl, 7.0 ppb Br and 0.2 ppb I, by assuming the fraction of the martian crust is approximately representative of the degree of partial melt (Taylor et al. 2010). Combined with estimates of Cl in the martian crust of 350 ppm (Taylor, 2010), and conservatively assuming the proportions in the martian crust are approximately chondritic, a BSM halogen composition of ~22 ppm Cl, ~74 ppb Br and ~6 ppb I is calculated. While the Cl is similar to estimates from

892 Taylor et al. (2010) of 32 ±9 ppm, our Br estimate is lower by a factor of ~2.5
893 (191 ±58 ppb). A comparison with estimates of bulk silicate Earth (25 ±9 ppm Cl,
894 74 ±26 ppb Br and 14 ±11 ppb I; McDonough and Sun, 1995; Clay et al., 2017)
895 suggests that the silicate portions of Mars and Earth have broadly similar bulk
896 halogen compositions. Previous work on the terrestrial halogen budget has
897 shown that terrestrial heavy halogens could be accounted for by accretion, not
898 precluding the later addition of halogens in a 'late veneer' event (Clay et al.
899 2017). The similarity of BSE and BSM halogen budgets might therefore suggest
900 a common carrier(s) or process(es) for halogen delivery to the terrestrial planets.
901

902 **Implications**

903 Our results suggest the enriched and depleted shergottite mantle sources
904 have a distinct halogen geochemical signature. This is consistent with previous
905 work suggesting heterogeneously distributed volatiles in the martian mantle (e.g.,
906 McCubbin et al. 2016). Given estimates that the enriched and depleted
907 shergottite mantle sources were distinct as early as ~4504 Ma (e.g., Borg et al.
908 2016), depleted and enriched shergottite halogen source compositions were
909 probably distinct early on in Mars' history. The martian surface is known to be
910 particularly Cl- and Br-rich (e.g., Gellert et al. 2004, 2006; Taylor et al. 2010),
911 largely due to the presence of salts and alteration assemblages on the surface.
912 However, the source of this surficial enrichment is unclear. A halogen-poor
913 depleted shergottite mantle source and a potential halogen-rich enriched mantle
914 shergottite source might indicate that some volatiles were transferred from the

915 mantle to crust early in Mars' history. Given the hydrophilic nature of the
916 halogens, the role of aqueous fluids would likely have been important in the
917 concentration and transportation of halogens to the early martian surface, a
918 similar process to what is suggested for sequestration of halogens in the surface
919 reservoirs on early Earth (Clay et al. 2017).

920 Another similar observation to Earth is that of the uncertainty surrounding
921 the bulk I composition of both the martian crust and mantle. Measurements of the
922 I composition of bulk and mineral phases in ancient crustal lithologies (e.g., as
923 represented by meteorite NWA 7034 and grouped stones) would usefully
924 improve our knowledge of the martian I budget. Finally, the early sequestration of
925 halogens into the martian surface has significant implications for the habitability
926 of Mars: while salts are generally thought to be important for life, an
927 overabundance may have a detrimental effect on wider planetary habitability
928 potential.

929

Acknowledgements

We acknowledge the NASA Antarctic Meteorite Working Group for providing shergottite samples: LAR 06319,64, LAR 12011,6, LAR 12095,8, and LAR 12240,6 (bulk) and LAR 06319,46, LAR 12011,22, LAR 12095,28, and LAR 12240,17 (thin sections). We thank Mr Christopher Griffin, who was funded by a Paneth Meteorite Trust summer internship (administrated by the Royal Astronomical Society), and University of Manchester student Mr Alejandro Leiva who assisted in collecting EMPA and SEM data for this study. John Cowpe and Lydia Fawcett are thanked for assistance with irradiation organization and instrument support. We acknowledge funding by EPSRC, award EP/M028097/1, which supports the JEOL JXA-8530F FEG-EPMA. This work was in parts supported by the European Research Council (ERC) FP7 'NOBLE' grant No. 267692 (C.J.B), Royal Society (grant RS/UF140190) and STFC (grant ST/R000751/1) (K.H.J., R.B.), and partially by the NCCR "Planet S", funded by the Swiss SNF (H.B.). We acknowledge editorial suggestions from Anita Cadoux and two constructive reviews by Lydia Hallis and Sami Mikhail, all of which improved an earlier version of the manuscript.

References cited

Aiuppa, A., Baker, D.R., and Webster, J.D. (2009) Halogens in volcanic systems. Chemical Geology, 263, 1–18.

Anders, E. and Grevesse, N. (1989) Abundances of the elements: Meteoritic and solar. Geochimica et Cosmochimica Acta, 53, 197–214.

Avice, G., Bekaert, D.V., Chennaoui Aoudjehane, H., and Marty, B. (2018) Noble gases and nitrogen in Tissint reveal the composition of the Mars atmosphere. Geochemical Perspective Letters, 6, 11–16.

Baird, A. K., Toulmin III, P., Clark, B.C., Rose Jr., H.J., Keil, K., Christian, R.P., and Gooding, J.L. (1976) Mineralogic and petrologic implications of Viking geochemical results from Mars: Interim results. Science, 194, 1288–1293.

Balta, J. B., Sanborn, M., Mcsween, H. Y., and Wadhwa, M. (2013) Magmatic history and parental melt composition of olivine-phyric shergottite LAR 06319: Importance of magmatic degassing and olivine antecrysts in Martian magmatism. Meteoritics and Planetary Sciences, 48, 1359–1382.

Balta, J. B., Tucker, K., Wadhwa, M., and McSween, H.Y. (2015a). Petrology and geochemistry of new Antarctic shergottites: LAR 12011, LAR 12095, and LAR 12240. 46th Lunar and Planetary Science Conference. Abstract #2294.

Balta, J. B., Sanborn, M. E., Udry, A., Wadhwa, M., and McSween, H. Y. (2015b). Petrology and trace element geochemistry of Tissint, the newest shergottite fall. Meteoritics and Planetary Sciences, 50, 63–85.

Basu Sarbadhikari, A., Day, J.M.D., Liu, Y., Rumble III, D., and Taylor, L.A. (2009) Petrogenesis of olivine-phyric shergottite Larkman Nunatak 06319: Implications for enriched components in martian basalts. Geochimica et Cosmochimica Acta, 73, 2190–2214.

Basu Sarbadhikari, A., Goodrich, C.A., Liu, Y., Day, J.M.D., and Taylor, L.A. (2011) Evidence for heterogeneous enriched shergottite mantle sources in Mars from olivine-hosted melt inclusions in Larkman Nunatak 06319. Geochimica et Cosmochimica Acta, 75, 6803–6820.

Basu Sarbadhikari, A., Babu, E.V.S.S.K., Vijaya Kumar, T., and Chennaoui Aoudjehane, H. (2016) Martian meteorite Tissint records unique petrogenesis among the depleted shergottites. Meteoritics and Planetary Science, 51, 1588–1610.

Bellucci, J.J., Whitehouse, M. J., John, T., Nemchin, A. A., Snape, J. F., Bland, P. A., and Benedix, G. K. (2017) Halogen and Cl isotopic systematics in Martian

993 phosphates: Implications for the Cl cycle and surface halogen reservoirs on
994 Mars. Earth and Planetary Science Letters, 458, 192–202.
995
996 Bogard D., Garrison D., and Park J. 2010. Chlorine abundances in Martian
997 meteorites. 41st Lunar and Planetary Science Conference. Abstract #1074
998
999 Bogard, D. D., Clayton, R. N., Marti, K., Owen, T. and Turner, G. (2001) Martian
1000 volatiles: isotopic composition, origin, and evolution. Space Science Reviews, 96,
1001 425–458.
1002
1003 Böhlke, J.K. and Irwin, J.J. (1992) Laser microprobe analyses of noble gas
1004 isotopes and halogens in fluid inclusions: Analyses of microstandards and
1005 synthetic inclusions in quartz. Geochimica et Cosmochimica Acta, 56, 187–201.
1006
1007 Borg L. E. and Draper D. S. (2003). A petrogenetic model for the origin and
1008 compositional variation of the Martian basaltic meteorites. Meteoritics and
1009 Planetary Science, 38, 1713–1731.
1010
1011 Borg, L. E., Brennecka, G. A. and Symes, S. J. K. (2016) Accretion timescale and
1012 impact history of Mars deduced from the isotopic systematics of martian
1013 meteorites. Geochimica et Cosmochimica Acta, 175, 150–167.
1014

Brandon, A. D., Puchtel, I. S., Walker, R. J., Day, J. M. D., Irving, A. J., and Taylor, L. A. (2012) Evolution of the Martian mantle inferred from the ^{187}Re–^{187}Os isotope and highly siderophile element abundance systematics of shergottite meteorites, Geochimica et Cosmochimica Acta, 76, 206-235.

Brandon, A.D., Ferdous, J., and Peslier, A.H. (2017) Evaluating crustal contamination effects on the lithophile trace element budget of shergottites. Goldschmidt Conference, Paris, 2017, Abstract #446.

Brazzle, R. H., Pravdivtseva, O. V, Meshik, A. P., and Hohenberg, C. M. (1999) Verification and interpretation of the I-Xe chronometer. Geochimica et Cosmochimica Acta 63, 739–760.

Brennecka G. A., Borg L. E., and Wadhwa M. (2014). Insights into the Martian mantle: The age and isotopics of the meteorite fall Tissint. Meteoritics and Planetary Science, 49, 412–418.

Bridges, J.C. and Warren, P.H. (2006) The SNC meteorites: basaltic igneous processes on Mars. Journal of the Geological Society, 163, 229-251.

Bridges J. C., Catling D. C., Saxton J. M., Swindle T. D., Lyon I. C., and Grady M. M. (2001). Alteration assemblages in Martian meteorites: Implications for near-surface processes. Space Science Reviews, 96, 365– 392.

Burgess R., Cartwright J. A., and Filiberto J. (2013). Halogen abundances of the Martian mantle. Mineralogical Magazine, 77(5) 793.

Busemann, H., Baur, H., and Wieler, R. (2000) Primordial noble gases in “phase Q” in carbonaceous and ordinary chondrites studied by closed-system stepped etching. Meteoritics and Planetary Science, 35, 949-973.

Cartwright, J.A., Ocker, K.D., Crowther, S.A., Burgess, R., and Gilmour, J.D. (2010) Terrestrial and Martian weathering signatures of xenon components in shergottite mineral separates. Meteoritics and Planetary Science, 45, 1359–1379.

Cartwright, J. A., Gilmour, J. D. and Burgess, R. (2013) Martian fluid and Martian weathering signatures identified in Nakhla, NWA 998 and MIL 03346 by halogen and noble gas analysis. Geochimica et Cosmochimica Acta, 105, 255–293.

Cartwright J. A., Ott U., Herrmann S., and Agee C. B. (2014) Modern atmospheric signatures in 4.4 Ga Martian meteorite NWA 7034. Earth and Planetary Science Letters, 400, 77-87

Chennaoui Aoudjehane H., Avice G., Barrat J. A., Boudouma O., Chen G., Duke M. J. M., Franchi I. A., Gattacceca J., Grady M. M., Greenwood R. C., Herd C. D.

K., Hewins R., Jambon A., Marty B., Rochette P., Smith C. L., Sautter V., Verchovsky A., Weber P. and Zanda B. (2012) Tissint Martian meteorite: a fresh look at the interior, surface, and atmosphere of Mars. Science, 338, 785–788.

Clay, P.L., Burgess, R., Busemann, H., Ruzié-Hamilton, L., Joachim, B., Day, J.M.D., and Ballentine, C.J. (2017) Halogens in chondritic meteorites and terrestrial accretion. Nature, 551, 614-618.

Crowther, S.A. and Gilmour, J.D. (2013) The Genesis solar xenon composition and its relationship to planetary xenon signatures. Geochimica et Cosmochimica Acta, 123, 17-34.

Day, J.M.D., Tait, K.T., McKay, D.S., Urdy, A., Moynier, F., Liu, Y., and Neal. C.R. (2018) Martian magmatism from plume metasomatized mantle. Nature Communications, 9, 4799.

Dreibus, G., and Wänke, H. (1985) Mars, a volatile-rich planet. Meteoritics, 20, 367–381.

Dreibus G. and Wänke, H. (1987). Volatiles on Earth and Mars—A comparison. Icarus, 71, 225–240.

Dreibus, G., Spettel, B., Wlotzka, F., Schultz, L., Weber, H. W., Jochum, K. P., and Wänke H. (1996). QUE 94201: An unusual Martian basalt. Meteoritics and Planetary Science, 31, A39–A40.

Dreibus, G., Spettel B., Haubold R., Jochum K. P., Palme H., Wolf, D., and Zipfel, J. (2000). Chemistry of a new shergottite: Sayh al Uhaymir 005. Meteoritics and Planetary Science, 35, A49–A49.

Dreibus G., Haubold R., Huisl W., and Spettel, B. (2003). Comparison of the chemistry of Yamato 980459 with DaG 476 and SaU 005. International symposium, Evolution of Solar System materials: A new perspective from Antarctic meteorites, 19–20.National Institute of Polar Research, Tokyo.

Dunham, E.T., Balta, J.B., Wadhwa, M., Sharp, T.G., and McSween, H.Y. (2019) Petrology and geochemistry of olivine-phyric shergottites LAR 12095 and LAR 12240: Implications for their petrogenetic history on Mars. Meteoritics and Planetary Science, 54, 811–835.

Ferrat, M., Weiss, D.J., Spiro, B., and Large, D. (2012) The inorganic geochemistry of a peat deposit on the eastern Qinghai-Tibetan Plateau and insights into changing atmospheric circulation in central Asia during the Holocene. Geochimica et Cosmochimica Acta, 91, 7-31.

1106 Filiberto J., Chin E., Day J. M. D., Franchi I. A., Greenwood R. C., Gross J.,
1107 Penniston-Dorland S. C., Schwenzer S. P., and Treiman A. H. (2012).
1108 Geochemistry of intermediate olivine-phyric shergottite Northwest Africa 6234,
1109 with similarities to basaltic shergottite Northwest Africa 480 and olivine-phyric
1110 shergottite Northwest Africa 2990. Meteoritics and Planetary Science, 47,1256–
1111 1273.
1112
1113 Filiberto, J., Gross, J., and McCubbin, F.M. (2016a) Constraints on the water,
1114 chlorine, and fluorine content of the Martian mantle. Meteoritics and Planetary
1115 Science, 51, 2023–2035.
1116
1117 Filiberto J., Baratoux D., Beaty D., Breuer D., Farcy B. J., Grott M., Jones J. H.,
1118 Kiefer W. S., Mane P., McCubbin F. M. and Schwenzer S. P. (2016b) A review of
1119 volatiles in the Martian interior. Meteoritics and Planetary Science, 51, 1935–
1120 1958.
1121
1122 Franz, H.B., Kim, S.-T., Farquhar, J., Day, J.D., Economos, R.C., McKeegan,
1123 K.D., Schmitt, A.K., Irving, A.J., Hoek, J. and Dottin III, J. (2014) Isotopic links
1124 between atmospheric chemistry and the deep sulphur cycle on Mars. Nature,
1125 508, 364–368.
1126

1127 Fritz, J., Greshake, A., and Stöffler, D. (2005) Micro-Raman spectroscopy of
1128 plagioclase and maskelynite in Martian meteorites: Evidence of progressive
1129 shock metamorphism. Antarctic Meteorite Research, 18, 96–116.
1130
1131 Funk, R.C. (2016) Petrology and geochemistry of new paired martian meteorites
1132 LAR 12240 and LAR 12095. 130 pp. M.S. Thesis, University of Houston,
1133 Houston, Texas.
1134
1135 Funk R. C., Brandon A. D., and Peslier A. (2015). Petrology and geochemistry of
1136 new paired Martian meteorites 12095 and 12240. 46th Lunar and Planetary
1137 Science Conference, Abstract #2830.
1138
1139 Gellert, R., Rieder, R., Anderson, R.C., Brückner, J., Clark, B.C., Dreibus, G.,
1140 Economou, T., Klingelhöfer, G., Lugmair, G.W., Ming, D.W., Squyres, S.W.,
1141 d'Uston, C., Wänke, H., Yen, A. and Zipfel, J. (2004) Chemistry of rocks and soils
1142 in Gusev crater from the alpha particle x-ray spectrometer. Science, 305, 829–
1143 832.
1144
1145 Gellert, R., Rieder, R., Brückner, J., Clark, B.C., Dreibus, G., Klingelhöfer, G.,
1146 Lugmair, G., Ming, D.W., Wänke, H., Yen, A., Zipfel, J., and Squyres, S.W.
1147 (2006) Alpha Particle X-Ray Spectrometer (APXS): Results from Gusev crater
1148 and calibration report. Journal of Geophysical Research, 111, E02S05.
1149

1150 Goettel, K.A. (1981) Density of the mantle of Mars. Geophysical Research
1151 Letters, 8, 497-500.
1152
1153 Goodrich C. A. 2002. Olivine-phyric Martian basalts: A new type of shergottite.
1154 Meteoritics and Planetary Science, 37, B31–B34.
1155
1156 Gregory, T., Joy, K. H., Strekopytov, S. and Curran, N. M. (2017), Geochemistry
1157 and petrology of howardite Miller Range 11100: A lithologically diverse piece of
1158 the Vestan regolith. Meteoritics and Planetary Science, 52, 206–224.
1159
1160 Hallis, L. J., Kemppinen, L., Lee, M. R. and Taylor, L. A. (2017) The origin of
1161 alteration “orangettes” in Dhofar 019: Implications for the age and aqueous
1162 history of the shergottites. Meteoritics and Planetary Science, 52, 2695–2706.
1163
1164 Herd C. D., Borg L. E., Jones J. H., and Papike J. J. (2002). Oxygen fugacity and
1165 geochemical variations in the Martian basalts: Implications for Martian basalt
1166 petrogenesis and the oxidation state of the upper mantle of Mars. Geochimica et
1167 Cosmochimica Acta, 66, 2025–2036.
1168
1169 Herd, C.D.K., Walton, E.L., Agee, C.B., Muttik, N., Ziegler, K., Shearer, C.K.,
1170 Bell, A.S., Santos, A.R., Burger, P.V., Simon, J.I., Tappa, M.J., McCubbin, F.M.,
1171 Gattacceca, J., Lagroix, F., Sanborn, M.E., Yin, Q-Z., Cassata, W.S., Borg, L.E.,
1172 and Caffee, M.W. (2017) The Northwest Africa 8159 martian meteorite:

1173 Expanding the martian sample suite to the early Amazonian. Geochimica et
1174 Cosmochimica Acta, 218, 1-26.
1175
1176 Holland, G. and Ballentine, C.J. (2006) Seawater subduction controls the heavy
1177 noble gas composition of the mantle. Nature, 441, 186-191.
1178
1179 Howarth, G. H., Liu, Y., Kohl, I., Pernet-Fisher, J. F., Wetterland, C., Chen Y.,
1180 Bodnar, R. J., Young, E. D., and Taylor, L. A. (2014). Heterogeneous olivine-
1181 phyric to pyroxene-phyric textures in paired shergottites LAR 12095 and LAR
1182 12240. 46th Lunar and Planetary Science Conference. Abstract #1360.
1183
1184 Howarth, G.H., Liu, Y., Chen, Y., Pernet-Fisher, J., and Taylor, L.A. (2016)
1185 Postcrystallization metasomatism in shergottites: Evidence from the paired
1186 meteorites LAR 06319 and LAR 12011. Meteoritics and Planetary Science, 51,
1187 2061–2072.
1188
1189 Irving, A. J., Kuehner, S. M., Tanaka, R., Herd, C. D. K., Chen, G., Lapen, T. J.
1190 (2012). The Tissint depleted permafic olivine phyric shergottite; petrologic,
1191 elemental and isotopic characterization of a recent fall in Morocco. 43rd Lunar
1192 and Planetary Science Conference, Abstract #2510.
1193

1194 Karlsson, H.R., Clayton, R.N., Gibson, E.K., Jr., and Mayeda, T.K (1992) Water
1195 in SNC meteorites: Evidence for a Martian hydrosphere. Science, 255, 1409–
1196 1411.
1197
1198 Keller, J.M., Boynton, W.V., Karunatillake, S., Baker, V.R., Dohm., J.M., Evans,
1199 L.G., Finch, M.J., Hahn, B.C., Hamara, D.K., Janes, D.M., Kerry, K.E., Newsom,
1200 H.E., Reedy, R.C., Sprague, A.L., Squyres, S.W., Starr, R.D., Taylor, G.J., and
1201 Williams, R.M.S. (2006) Equatorial and midlatitude distribution of chlorine
1202 measured by Mars Odyssey GRS. Journal of Geophysical Research, 111
1203 E03S08.
1204
1205 Kendrick, M. A. (2012) High precision Cl, Br and I determinations in mineral
1206 standards using the noble gas method. Chemical Geology, 292–293, 116–126.
1207
1208 Kendrick, M.A., Kamenetsky, V., Phillips, D., and Honda, M. (2012) Halogen
1209 systematics (Cl, Br, I) in Mid-Ocean Ridge Basalts: a Macquarie Island case
1210 study. Geochimica et Cosmochimica Acta, 81, 82–93.
1211
1212 Kendrick, M.A., Arculus, R., Burnard, P., and Honda, M. (2013) Quantifying brine
1213 assimilation by submarine magmas: Examples from the Galápagos Spreading
1214 Centre and Lau Basin. Geochimica et Cosmochimica Acta, 123, 150-165.

1215 Kendrick, M.A., Jackson, M.G., Kent, A. J.R., Hauri, E.H., Wallace, P.J., and
1216 Woodhead, J., (2014). Contrasting behaviours of CO_2, S, H_2O and halogens (F,

1217 Cl, Br, and I) in enriched-mantle melts from Pitcairn and Society seamounts.
1218 Chemical Geology, 370, 69-81.
1219
1220 Langenauer, M. and Krähenbühl, U. (1993) Depth-profiles and surface
1221 enrichment of the halogens in four Antarctic H5 chondrites and in two non-
1222 Antarctic chondrites. Meteoritics, 28, 98–104.
1223
1224 Lapen, T. J., Righter, M., Andreasen, R., Irving, A. J., Satkoski, A. M., Beard, B.
1225 L., Nishiizumi, K., Jull, A. J. T., and Caffee, M. W. (2017) Two Billion Years of
1226 Magmatism Recorded from a Single Mars Meteorite Ejection Site, Science
1227 Advances 3, e1600922.
1228
1229 Leya I. and Masarik J. (2009) Cosmogenic nuclides in stony meteorites revisited.
1230 Meteoritics and Planetary Science, 44, 1061-1086.
1231
1232 Li, Y-H. (1991) Distribution patterns of the elements in the ocean: A synthesis.
1233 Geochimica et Cosmochimica Acta 55, 3223–3240.
1234
1235 Lodders, K. (1998). A survey of shergottite, nakhlite and chassigny meteorites
1236 whole-rock compositions. Meteoritics and Planetary Science, 33, 183–190.
1237
1238 Mahaffy, P.R., Webster, C.R., Atreya, S.K., Franz, H., Wong, M., Conrad, P.G.,
1239 Harpold, D., Jones, J.J., Leshin, L.A., Manning, H., Owen, T., Pepin, R. O.,

Squyres, S., Trainer, M., MSL Science Team (2013) Abundance and isotopic composition of gases in the Martian Atmosphere from the Curiosity Rover. Science, 341, 263-266.

McBride, K., McCoy, T., LaCroix, L., Welzenbach, L., and Sharp, Z. (2007) New meteorites: 2004-2006 collection. Antarctic Meteorite Newsletter, 30 (2), 5-30.

McBride, K., Harrington, R., Satterwhite, C., Corrigan, C., Singerling, S., Beck, A., Welzenbach, L., and McCoy, T. (2013) New meteorites: 2010 and 2012 collection. Antarctic Meteorite Newsletter, 36 (2), 4-20.

McCubbin F.M., Boyce J.W., Srinivasan P., Santos A. R., Elardo S.M., Filiberto J., Steele A. and Shearer C.K. (2016) Heterogeneous distribution of H_2O in the Martian interior: Implications for the abundance of H_2O in depleted and enriched mantle sources. Meteoritics and Planetary Science, 51, 2036–2060.

McDonough, W.F. and Sun, S-s. (1995) The composition of the Earth. Chemical Geology, 120, 223-253.

Meyer, C. (2014) Mars Meteorite Compendium. Astromaterials Research and Exploration Science (ARES), Johnson Space Center, JSC #27672 Revision C.

1262 Mikouchi T. and Takenouchi A. (2014) Mineralogy and petrology of LAR 12095
1263 olivine-phyric shergottite: A possible launch pair from Mars with Dar al Gani 476
1264 and Sayh Al Uhaymir 005. 45th Lunar and Planetary Science Conference,
1265 Abstract #1858.
1266
1267 Milman-Barris M., Beckett J., Baker M., Hofmann A., Morgan Z., Crowley M.,
1268 Vielzeuf D., and Stolper E. (2008) Zoning of phosphorus in igneous olivine.
1269 Contributions to Mineralogy and Petrology, 155, 739–765.
1270
1271 Mittlefehldt D. W., Lindstrom D. J., Lindstrom M. M. and Martinez R. R. (1999) An
1272 impact-melt origin for lithology A of Martian meteorite Elephant Moraine A79001.
1273 Meteoritics and Planetary Science, 34, 357–367.
1274
1275 Nagao, K. and Park, J. (2008) Noble gases and cosmic-ray exposure ages of two
1276 Martian Shergottites, RBT 04262 and LAR 06319 recovered in Antarctica.
1277 Meteoritics and Planetary Science, 43, A107.
1278
1279 Nyquist, L.E., Bogard, D.D., Shih, C-Y., Greshake, A., Stöffler, D. and Eugster,
1280 O. (2001) Ages and geologic history of martian meteorites. Chronology and
1281 Evolution of Mars 96, 105-164.
1282

Ocker, K.D. and Gilmour, J.D. (2004) Martian xenon components in Shergotty mineral separates: Locations, sources, and trapping mechanisms. Meteoritics and Planetary Science, 39, 1967–1981.

Orosei, R., Lauro, S.E., Pettinelli, E., Cicchetti, A., Coradini, M., Cosciotti, B., DiPaolo, F., Flamini, E., Mattei, E., Pajola, M., Soldovieri, F., Cartacci, M., Cassenti, F., Frigeri, A., Giuppi, S., Martifi, R., Masdea, A., Mitri, G., Nenna, C., Noschese, R., Restani, M, and Seu, R. (2018) Radar evidence of subglacial liquid water on Mars. Science, 361, 490–493.

Park, J., Bogard, D. D., Nyquist, L. E., Garrison, D. H., and Mikouchi, T. (2013) Ar-Ar ages and trapped Ar components in Martian shergottites RBT 04262 and LAR 06319. Geochimica et Cosmochimica Acta, 121, 546–570.

Peslier A. H., Hnatyshin D., Herd C. D. K., Walton E. L., Brandon A., Lapen T. J. and Shafer J. T. (2010) Crystallization, melt inclusion, and redox history of a martian meteorite: olivine-phyric shergottite Larkman Nunatak 06319. Geochimica et Cosmochimica Acta, 74, 4543–4576.

Rampe, E.B., Cartwright, J.A., McCubbin, F.M., and Osterloo, M.M. (2018) The Role of halogens during fluid and magmatic processes on Mars, In D.E. Harlov and L. Aranovich, (Eds) The Role of Halogens in Terrestrial and Extraterrestrial Geochemical Processes, pp. 959-995, Springer Geochemistry.

Rao, M.N., Sutton, S.R., McKay, D.S., and Dreibus, G. (2005) Clues to Martian brines based on halogens in salts from nakhlites and MER samples. Journal of Geophysical Research, 110, E12S06.

Renne, P. R., Mundil, R., Balco, G., Min, K. and Ludwig, K. R. (2010) Joint determination of ^{40}K decay constants and $^{40}Ar^{*}/^{40}K$ for the Fish Canyon sanidine standard, and improved accuracy for $^{40}Ar/^{39}Ar$ geochronology. Geochimica et Cosmochimica Acta, 74, 5349–5367.

Riebe, M. E. I., Welten, K. C., Meier, M. M. M., Wieler, R., Bart, M. I. F., Ward, D., Laubenstein, M., Bischoff, A., Caffee, M. W., Nishiizumi, K., and Busemann, H. (2017) Cosmic-ray exposure ages of six chondritic Almahata Sitta fragments. Meteoritics and Planetary Science, 52, 2353-2374.

Righter, M., Andreasen, R., and Lapen, T.J. (2015) Lu-Hf and Sm-Nd systematics of martian meteorites Larkman Nuntak 12011 and 12095. 46th Lunar and Planetary Science Conference, Abstract #2889.

Ruzié-Hamilton, L., Clay, P.L., Burgess, R., Joachim, B., Ballentine, C.J., and Turner, G. (2016) Determination of halogen abundances in terrestrial and extraterrestrial samples by the analysis of noble gases produced by neutron irradiation. Chemical Geology, 437, 77–87.

Saal A. E., Hauri E. H., Langmuir C. H., and Perfit M. R. (2002). Vapour undersaturation in primitive mid-ocean-ridge basalt and the volatile content of Earth's upper mantle. Nature, 419, 451–455.

Shafer, J. T., Brandon, A. D., Lapen, T. J., Righter, M., Peslier, A. H., and Beard, B. L. (2010) Trace element systematics and ^{147}Sm-^{143}Nd and ^{176}Lu-^{176}Hf ages of Larkman Nunatak 06319: Closed-system fractional crystallization of an enriched shergottite magma. Geochimica et Cosmochimica Acta, 74, 7307-7328.

Shih C-Y., Nyquist L.A. and Reese Y. (2009) Rb-Sr and Sm-Nd studies of olivine-phyric Shergottites RBT 04262 and LAR 06319: Isotopic evidence for relationship to enriched basaltic shergottites. 40th Lunar and Planetary Science Conference, Abstract #1360.

Shirai, N. and Ebihara, M. (2004). Chemical characteristics of a Martian meteorite, Yamato 980459. Antarctic Meteorite Research 17, 55–67.

Stamenković, V., Ward, L.M., Mischna, M., and Fischer, W.W. (2018) O_2 solubility in Martian near-surface environments and implications for aerobic life. Nature Geoscience, 11, 905–909.

1351 Steele, A., Benning, L.G., Wirth, R., Siljeström, S., Fries, M.D., Hauri, E., Conrad,
1352 P.G., Rogers, K., Eigenbrode, J., Schreiber, A., Needham, A., Wang, J.H.,
1353 McCubbin, F.M., Kilcoyne, D., and Rodriguez Blanco, J.D. (2018) Organic
1354 synthesis on Mars by electrochemical reduction of CO_2. Science Advances, 4,
1355 eaat5118.
1356
1357 Strekopytov, S.V. and Dubinin, A.V. (1997) Determination of Zr, Hf, Mo, W and
1358 Th in standard reference samples of ocean sediments by inductively coupled
1359 plasma mass spectrometry. Journal of Analytical Chemistry 52, 1171.
1360
1361 Symes S. J., Borg L. E., Shearer C. K., and Irving A. J. (2008). The age of the
1362 Martian meteorite Northwest Africa 1195 and the differentiation history of the
1363 shergottites. Geochimica et Cosmochimica Acta 72,1696–1710.
1364
1365 Takenouchi, A., Mikouchi, T., and Yamaguchi, A. (2018) Shock veins and brown
1366 olivine in Martian meteorites: Implications for their shock pressure–temperature
1367 histories. Meteoritics and Planetary Science 53, 2259–2284.
1368
1369 Taylor, G.J., Boynton, W.V., McLennan, S.M., and Martel, L.M.V. (2010) K and Cl
1370 concentrations on the Martian surface determined by the Mars Odyssey Gamma
1371 Ray Spectrometer: Implications for bulk halogen abundances in Mars.
1372 Geophysical Research Letters, 37, L12204.
1373

Usui T., McSween H. Y. and Floss C. (2008) Petrogenesis of olivine-phyric shergottite Yamato 980459, revisited. Geochimica et Cosmochimica Acta, 72, 1711–1730.

Wänke, H., and G. Dreibus (1994) Chemistry and accretion history of Mars. Philosophical Transactions of the Royal Society Series A, 349, 285–293.

Watson, E.B., Cherniak, D.J. and Holycross, M.E. (2015) Diffusion of phosphorus in olivine and molten basalt. American Mineralogist, 100, 2053–2065.

Welsch, B., Hammer, J., and Hellebrand, E. (2014) Phosphorus zoning reveals dendritic architecture of olivine, Geology, 42, 867–870.

Wieler, R. (2002) Cosmic-ray-produced noble gases in meteorites. Reviews in Mineralogy and Geochemistry, 47, 125-170.

Wieler, R., Huber, L., Busemann, H., Seiler, S., Leya, I., Maden, C., Masarik, J., Meier, M.M.M., Nagao, K., Trappitsch, R., and Irving, A.J. (2016) Noble gases in 18 Martian meteorites and angrite Northwest Africa 7812—Exposure ages, trapped gases, and a re-evaluation of the evidence for solar cosmic ray-produced neon in shergottites and other achondrites. Meteoritics and Planetary Science, 51, 407–428.

Wiens, R. C., Becker, R. H. and Pepin, R. O. (1986) The case for a martian origin of the shergottites, II. Trapped and indigenous gas components in EETA 79001 glass. Earth and Planetary Science Letters, 77, 149-158.

Williams J. T., Shearer C. K., Sharp Z. D., Burger P. V., McCubbin F. M., Santos A. R., Agee C. B. and McKeegan K. D. (2016) The chlorine isotopic composition of Martian meteorites 1: Chlorine isotope composition of Martian mantle and crustal reservoirs and their interactions. Meteoritics and Planetary Science, 51, 2092–2110.

Zipfel J., Scherer P., Spettel B., Dreibus G., and Schultz L. (2000). Petrology and chemistry of the new shergottite Dar al Gani 476. Meteoritics and Planetary Science, 35, 95–106.

Figure Captions

Figure 1. Qualitative false color map of (a) Mg, (b) Ca, (c) Al and (d) P in the Tissint shergottite meteorite in counts per second, measured on the JEOL JXA-8530F at the University of Manchester. The same portion of the section is imaged in each panel, comprising central olivine grains in a matrix of pyroxene with variable Ca compositions. The olivine grains show gradients in Mg abundance (a) from core to rim and pronounced P-zonation (d). Map conditions: 15 kV acceleration voltage, 1 µm beam, 495 nA beam current, 512 x 512 pixels, 400 ms/pixel, 2 µm/pixel.

Figure 2. Multi-element (a) and rare earth element (b) distribution patterns from enriched shergottite pair LAR 06139, LAR 12011 and depleted shergottite pair LAR 12240 and LAR 12095 from this study, normalized to CI chondrite. Tissint data is shown for comparison as reported in the studies of Avice et al. (2018), Balta et al. (2015), Chennaoui Aoudjehane et al. (2012) and Irving et al. (2012). Normalization values for CI chondrite are from Anders and Grevesse (1989).

Figure 3. Calculated mineral compositions of (a) maskelynite, (b) pyroxene, (c) calculated range of Fo-content of measured olivine and (d) CaO (wt.%) as a function of calculated Fo-content in shergottite samples from this study. Reference mineral compositions from LAR 06139 are shown as grey circles and reference compositions from LAR 12240/12095 are shown as grey diamonds

(Balta et al. 2013, 2015; Basu Sarbadhikari et al. 2009, 2011,2016; Dunham et al. 2019).

Figure 4. Bromine (ppb) (a), I (ppb) (b) and K (ppm) (c) abundances as a function of Cl (ppm) in martian shergottite meteorites from this study. Log scales are used to accommodate the range in observed concentrations and insets focused on the samples measured in this study to highlight variation between samples. Reference data, including the range of measured Cl concentrations from LAR 12011/06319 apatite (Howarth et al. 2016), regolith breccia NWA 7355 apatite (Bellucci et al. 2017), measured and calculated Mars Odyssey GRS data (Taylor et al. 2010), Mars exploration rover (MERA/MERB) surface data (Gellert et al. 2004, 2006) and measurements of SNC meteorites (Dreibus and Wänke, 1987; Dreibus et al. 2006; Cartwright et al. 2013) are plotted for comparison. BSE and carbonaceous chondrite composition (white stars, reported in Clay et al. 2017) and BSM composition (black star, calculated) are given for reference.

Figure 5. I/Cl (wt. $\times 10^{-3}$) as a function of Br/Cl (wt. $\times 10^{-3}$) in martian shergottite samples measured in this study compared with reference martian, meteoritic and terrestrial material. The grey box is representative of the terrestrial mantle array as defined by measurement of mid-ocean ridge and ocean island basalt glasses (Kendrick et al., 2012, 2013, 2014). Data sources for reference compositions are given in the caption to Figure 4. BSE and carbonaceous chondrite composition

(white stars, reported in Clay et al. 2017) and BSM composition (black star, calculated) are given for reference.

Figure 6. Neon three isotope plot showing the four data points for the LAR samples measured in the work and data for Tissint (Wieler et al. 2016). All samples contain dominantly cosmogenic GCR-derived Ne. LAR 06319 and 12011 are paired and distinct from paired LAR 12240 and 12095. Only in the former a small trapped Ne component is present, which could be air, in view of the Kr and Xe air contaminations found also in these shergottites. The latter show an additional SCR-derived component.

Figure 7. (a) Cl (ppm) as a function of La (ppm) abundance in martian depleted and enriched shergottites from this study with reference data for depleted intermediate and enriched shergottites shown. Cl and La are determined in this study with the exception of the La abundance for Tissint, which is an average (1σ S.D.) of the reported values in Balta et al. (2015), Chennaoui Aoudjehane et al. (2012) and Irving et al. (2012). (b) Close up of the data from this study on a linear scale to highlight the variation between pairs. The terrestrial Cl/La (21.5) and martian Cl/La (~ 52.5) ratios are reported in Filiberto et al. (2016). The Cl range for abraded Gusev basalts is shown and taken to represent martian surface basalts with surface coatings or alteration removed (i.e., abraded/'ratted' by the rock abrasion tool; Gellert et al. 2006). The Cl range for unabraded Gale basalts is shown and taken to represent Cl abundances present in martian surface

alteration products (Schmidt et al., 2014). Low Cl/La ratios may indicate degassing and high Cl/La ratios may indicate alteration or contamination. (c) Chlorine as a function of bulk P_2O_5 (wt.%) in depleted and enriched shergottites. Bulk P_2O_5 for Tissint is from Avice et al. (2108). Rather than a correlation between Cl and P_2O_5, which would indicate apatite as a sole carrier of Cl in these samples, we observe grouping of enriched samples with high Cl and P_2O_5 compared to lower Cl and P_2O_5 in depleted shergottites. Reference data for previous shergottite studies from the following sources: Dreibus et al. (1996); Dreibus et al. (2003); Shirai and Ebihara (2004); Zipfel et al. (2000); Dreibus et al. (2000); Burgess et al. (2013); Dreibus and Wänke (1985, 1987); Bogard et al. (2010); Cartwright et al. (2013); Lodders (1998); Filiberto et al. (2012); Meyer (2014).

Figure 8 The potential contribution of apatite on the (a) Cl (b) Br and (c) I to the bulk halogen budget of depleted and enriched shergottite meteorites in this study. “Enriched” (red line) and “depleted” (blue line) apatite compositions are from Bellucci et al. (2017) represented by an average composition of LAR 12011 and a single measurement of SaU 005, respectively. The grey field shows the range of halogen compositions of enriched shergottites in this study, the grey field bounded by dashed black line represents the range for depleted shergottites and the solid black line is the average composition of Tissint. Apatite is likely the dominant halogen host but cannot account for Cl, Br and I abundances or proportions in all samples. There is likely a much wider range of halogen

compositions in martian apatite that may account for the bulk composition, however interpretation is currently limited by a paucity of complete Cl, Br and I measurements of apatite.

Figure 9 CI-chondrite normalized halogen abundances for shergottite samples measured in this study. CI chondrite data (black line) is from Clay et al. (2017) and shergottite reference lines (grey dashed lines) are from Dreibus and Wänke (1987).

Supplementary Appendix Table Captions

Table S1. ICP-MS and ICP-OES major and trace element data for standard reference materials and limits of quantification for each element.

Table S2. EPMA determined pyroxene (a), olivine (b), minor spinel, ilmenite and sulfide (d) and glass (e) compositions for shergottite samples Tissint, LAR 06319, LAR 12011, LAR 12095, and LAR 12240.

Table S3. Ar-Ar data, irradiation parameters and correction factors used in Ar-Ar age and halogen data reduction for shergottite samples Tissint, LAR 06319, LAR 12011, LAR 12095, and LAR 12240.

Table S4. Helium, Ne, Ar (in 10^{-8} cm^3 STP/g), Kr and Xe (in 10^{-10} cm^3 STP/g) concentrations and isotopic ratios in LAR 06319, LAR 12011, LAR 12095, and LAR 12240. Uncertainties of concentrations include those of counting statistics, sample masses, blanks and detector sensitivity. Uncertainties of isotopic ratios include those of counting statistics, blank corrections, and instrumental mass discrimination. Uncertainties of cosmogenic and trapped concentrations include the uncertainties of the deconvolution, i.e., the choice of the endmember components and all experimental uncertainties.

Tables

Table 1. Summary description of sample information for Tissint, and pairs LAR 06319/12011 and LAR 12095/12240.

Sample	Type	REE Classification	Modal Mineralogy (vol. %)	Crystallisation Age (Ma)	CRE Age (Ma)
Tissint	Olivine-phyric shergottite	Depleted	25-28% olivine 50-52% pyroxene 25-28% maskelynite 1-2% phosphates, oxides and sulfides [1]	574 ±20 [4]	0.7±0.3 [5]
LAR 12095/ 12240	Olivine-phyric shergottite	Depleted	16-17% olivine 61-62% pyroxene 21-22% as maskelynite 1% phosphates, oxides and sulfides [2]	NA but ~ 400-550 Ma estimate [6]	0.84±0.15 (this work)
LAR 12011/ 06139	Olivine-phyric shergottite	Enriched	~24% olivine 54% pyroxene ~18% maskelynite 2.1% phosphates, 1.3% oxides and 0.3% sulfides [3]	163 ±13 Ma – 207 ±14 Ma [7-9]	2.4-3.3 [7,10] 0.35±0.05 (this work)
Refs.: [1] Balta et al. 2015b [2] Dunham et al., 2019 [3] Basu Sarbadhikari et al. (2009) [4] Brennecka et al., (2014) [5] Chennaoui Aoudjehane et al. (2012) [6] Righter et al. (2015) [7] Park et al. (2013) [8] Shih et al. (2009) [9] Shafer et al. (2010) [10] Nagao and Park (2008)					

Table 2. Bulk rock major and trace element composition of shergottite samples LAR 06319, LAR 12011, LAR 12095, and LAR 12240, measured by ICP-MS and ICP-OES at the Natural History Museum, London. Major elements are reported as wt. % and trace elements as ppm. Uncertainties are reported as 2σ standard deviation. Standard reference material data and detection limits are reported in Table S1.

	unit	*n*	LAR12095	±(2σ S.D.)	LAR12240	±	LAR06319	±	LAR12011	±
SiO_2	wt%	3	47.6	0.4	48.0	0.3	45.3	0.4	45.7	0.5
TiO_2	wt%	3	0.445	0.008	0.519	0.012	0.692	0.029	0.719	0.032
Al_2O_3	wt%	3	5.35	0.19	5.92	0.16	5.55	0.29	5.94	0.30
Cr_2O_3	wt%	3	0.884	0.022	0.898	0.005	0.625	0.002	0.578	0.004
Fe_2O_3	wt%	3	19.3	0.6	18.7	0.4	22.8	1.15	22.4	1.13
MnO	wt%	3	0.46	0.01	0.45	0.01	0.501	0.028	0.46	0.03
MgO	wt%	3	18.17	0.35	17.10	0.42	15.86	0.59	15.32	0.56
CaO	wt%	3	6.10	0.18	6.50	0.17	6.36	0.26	6.55	0.32
Na_2O	wt%	3	0.75	0.03	0.84	0.03	1.09	0.07	1.17	0.07
K_2O	wt%	3	0.014	0.002	0.0163	0.001	0.142	0.010	0.139	0.014
P_2O_5	wt%	3	0.341	0.004	0.408	0.004	0.718	0.017	0.756	0.018
TOTAL	wt%		99.49		99.29		99.69		99.74	
Li	ppm	3	1.55	0.07	1.526	0.03	3.28	0.04	3.392	0.084
Be	ppm	3	0.0196	0.0012	0.0228	0.0012	0.277	0.009	0.282	0.01
K	ppm	3	113	13	135	11	1175	87	1153	119
Sc	ppm	5	33.6	2.8	34.9	3.8	35.4	2.7	34.9	3.3
V	ppm	5	191	4	188	10	218	7	213	11
Cr	ppm	3	6051	150	6145	37	4276	12	3954	24
Co	ppm	5	56.2	0.89	52.4	1.9	56.0	1.0	54.0	2.02
Ni	ppm	5	262	5	233	10	213	4	204	9
Cu	ppm	5	7.43	0.21	6.93	0.18	8.78	0.26	8.28	0.20
Zn	ppm	5	63.1	1.8	61.7	3.7	76.6	2.2	74.9	3.53
Ga	ppm	4	11.4	0.5	12.5	0.3	14.0	0.3	14.1	0.45
Rb	ppm	7	0.226	0.496	0.278	0.051	5.45	0.30	5.49	0.25
Sr	ppm	4	19.5	2.17	27.4	0.76	41.5	2.109	41.3	1.08
Y	ppm	5	8.6	1.63	9.94	0.65	13.8	0.597	14.2	0.82

Zr	ppm	5	11.0	5.98	17.8	0.44	47.2	1.431	51.6	2.99
Nb	ppm	5	0.156	0.30	0.185	0.02	3.53	0.119	3.56	0.15
Mo	ppm	3	0.058	0.03	0.176	0.01	0.109	0.007	0.188	0.02
Cd	ppm	5	0.019	0.01	0.019	0.01	0.017	0.006	0.0215	0.00
Cs	ppm	4	0.0111	0.03	0.0082	0.00	0.341	0.019	0.337	0.01
Ba	ppm	4	1.77	0.44	2.7	0.14	24.3	0.7	25.2	0.2
Hf	ppm	5	0.491	0.39	0.709	0.08	1.43	0.114	1.56	0.20
Ta	ppm	5	<0.015	0.09	<0.015	nd	0.133	0.032	0.138	0.05
W	ppm	3	<0.1	0.02	<0.1	nd	0.417	0.022	0.351	0.01
Tl	ppm	4	0.0061	0.00	0.0116	0.00	0.0149	0.003	0.0148	0.00
Pb	ppm	5	0.110	0.20	0.178	0.10	0.405	0.100	0.359	0.10
Th	ppm	5	0.0197	0.08	0.0218	0.01	0.389	0.034	0.405	0.04
U	ppm	5	0.0068	0.02	0.0099	0.01	0.097	0.011	0.102	0.01
La	ppm	5	0.124	0.285	0.152	0.031	2.02	0.08	2.08	0.143
Ce	ppm	5	0.383	0.859	0.455	0.075	4.84	0.31	5.01	0.429
Pr	ppm	5	0.0758	0.120	0.0871	0.017	0.716	0.062	0.732	0.060
Nd	ppm	5	0.575	0.384	0.681	0.049	3.62	0.19	3.77	0.19
Sm	ppm	5	0.470	0.318	0.561	0.054	1.38	0.11	1.42	0.16
Eu	ppm	5	0.272	0.086	0.307	0.031	0.531	0.025	0.551	0.043
Gd	ppm	5	1.18	0.33	1.38	0.13	2.26	0.11	2.35	0.17
Tb	ppm	5	0.240	0.09	0.279	0.03	0.412	0.026	0.430	0.04
Dy	ppm	5	1.73	0.34	1.99	0.19	2.79	0.14	2.89	0.17
Ho	ppm	5	0.364	0.12	0.423	0.04	0.573	0.044	0.591	0.06
Er	ppm	5	1.09	0.31	1.25	0.13	1.656	0.111	1.71	0.16
Tm	ppm	5	0.156	0.054	0.177	0.025	0.233	0.020	0.240	0.027
Yb	ppm	5	1.00	0.32	1.15	0.12	1.45	0.114	1.53	0.16
Lu	ppm	5	0.142	0.050	0.163	0.017	0.206	0.014	0.215	0.025
**Blank concentration of Pb is subtracted from Pb values*										

1552 Table 3. NI-NGMS determined heavy halogen (Cl, Br and I) abundances for shergottite samples Tissint, LAR 06319, LAR
1553 12011, LAR 12095, and LAR 12240. Irradiation parameters and correction factors are reported in Supplementary Table
1554 S3. Cl, K and Ba are reported as ppm and Br and I as ppb, with an uncertainty that encompasses corrections for mass
1555 discrimination, blank corrections and corrections for radioactive decay and interference reactions during irradiation of
1556 samples. The error reported for the average composition of Tissint is a 1σ standard deviation (n=6 for Cl, n=4 for Br and
1557 I). Reported ratios are by weight.
1558

Sample	Split	Mass (mg)	Cl (ppm)	Br (ppb)	I (ppb)	K (ppm)	Ba (ppm)	K/Cl (wt.)	Br/Cl (wt.) $\times10^{-3}$	I/Cl (wt.) $\times10^{-3}$	Ref.
Tissint	H-1	3.3	15.9±3.4	116±25	3.7±0.7	229±41	1.6±0.3	14.4±2.6	7.3±0.3	0.23±0.07	This work
Tissint	H-2	3.3	19.7±4.2	103±22	5.7±1.1	273±48	1.3±0.3	13.9±2.5	5.2±0.2	0.29±0.08	This work
Tissint	H-3	5.7	25.2±5.3	136±29	4.9±0.9	291±52	1.9±0.4	11.6±2.1	5.4±0.2	0.19±0.06	This work
Tissint	H-4	8.1	26.0±5.5	128±27	3.4±0.7	290±51	1.9±0.4	11.2±2	4.9±0.2	0.13±0.04	This work
Tissint	D-1†	6.7	20.5±4.3	nd		246±44	nd	12±3.3	nd		This work
Tissint	D-2†	7.1	19.9±4.2	nd		257±45	nd	12.9±3.5	nd		This work
Avg. Tissint			21.2±3.8	120.8±14.3	4.4±1.1	265±25	1.7±0.3	12.7±1.3	5.7±1.1	0.21±0.07	This work
LAR12240,6	A	2.40	15.8±0.8	62±4	329±22	174±6	2±0.2	11±0.4	3.9±0.3	20.8±1.7	This work
LAR 12240,6	B	4.43	10.1±0.5	46±3	259±17	133±4	1.5±0.1	13.1±0.4	4.5±0.4	25.6±2.1	This work
LAR 12095,8	C	2.37	13.0±0.6	54±4	78±5	149±5	1.8±0.2	11.5±0.4	4.1±0.4	6.1±0.5	This work
LAR 12095,8	I	3.14	15.0±0.7	58±4	59±4	145±5	1.9±0.2	9.6±0.3	3.9±0.3	3.97±0.3	This work
LAR 12011,6	6A	2.21	73.5±3.5	1303±91	152±10	911±31	19±1.5	12.4±0.4	17.7±1.5	2.07±0.2	This work

LAR 12011,6	6B	3.50	103.7±4.9	1624±113	198±13	1171±39	22.7±1.8	11.3±0.4	15.7±1.3	1.91±0.2	This work
LAR 06319,64	I	2.97	nd	1213±94	1423±95	745±25	15.9±1.3	nd	nd	nd	This work
LAR 06319,64	B	2.56	136.1±6.4	3061±215	4±1	1808±61	25±2	13.3±0.4	22.5±1.9	0.03±0.01	This work
For Reference	*Note*										
Carbonaceous Chondrite	Avg, 1σ S.D.		111±38	362±39	38±3	560		5.05	3.3±1.2	0.28±0.1	[1]
BSE	Avg, 1σ S.D.		25±9	74±26	14±11				3±1.5	0.56±0.48	[1]
Terrestrial Mantle*	Range		~1-1600	~1-5900	~2-1000	~200-52000			2.9±0.6	0.06±0.03	[2-4]
Seawater			18800	67000	58	390		0.02	3563	3.08	[5]
Martian Surface											
Gusev soil			5100	20000		3740					
Average martian soils (n=11)**	Avg, 1σ S.D.		5300	40000		3407					[6]
APXS MERA/B	Range		100-21300	6000-498000		40-12200					[7]
Odyssey GRS Surface^			390	2200	260	305					[8]
Martian Meteorites											
Shergottites (n=6)			14-145	69-890	12-960				4.9-10.8	0.03-122	[9]
Nakhlites (n=7)			101-563	80--950	15-1590				0.79-9.1	0.04-6.4	[10,11]
Chassigny (n=1)			34	97	10				2.85	0.29	[9]
References: [1] Clay et al (2017); [2] Kendrick et al. (2012); [3] Kendrick et al. (2013); [4] Kendrick et al. (2014); [5] Li (1991) [6] Gellert et al. (2004) [7] Gellert et al. (2006); [8] Taylor et al. 2010; [9] Dreibus and Wänke (1987); [10] Dreibus et al. (2006) [11] Cartwright et al. (2013)											
**Terrestrial mantle array defined by MORB and OIB glass analyses from [2-4]. **Average of 11 soils from Viking 1,2, Pathfinder and Gusev landing sites reported in [6]. †Tissint D-1 and D-2 were splits for Ar-Ar dating and therefore only Cl, K and not Br and I were determined. ^K and Cl are measured and Br and I calculated.*											

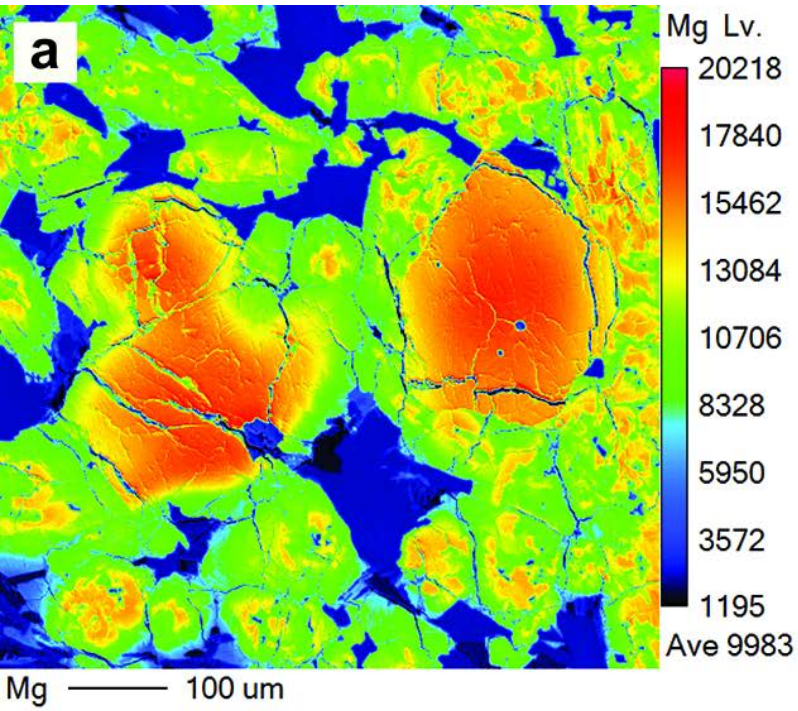
a
Mg Lv.
20218
17840
15462
13084
10706
8328
5950
3572
1195
Ave 9983
Mg 100 um

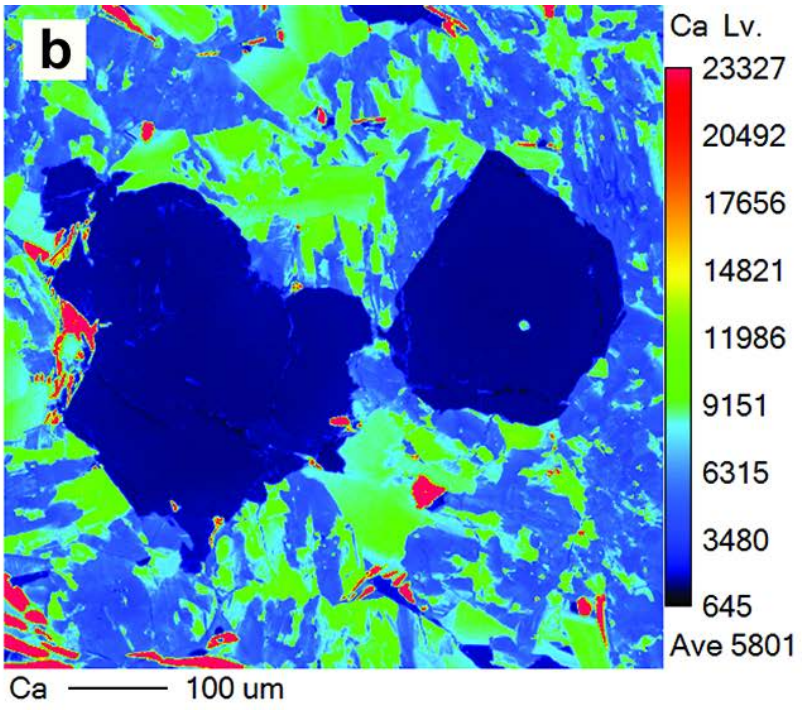
b
Ca Lv.
23327
20492
17656
14821
11986
9151
6315
3480
645
Ave 5801
Ca 100 um

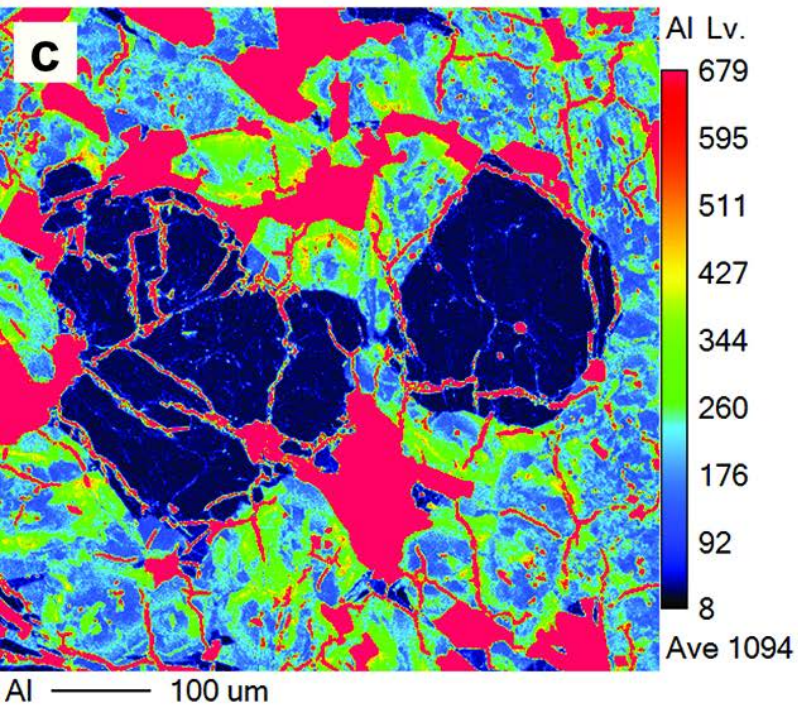
c
Al Lv.
679
595
511
427
344
260
176
92
8
Ave 1094
Al 100 um

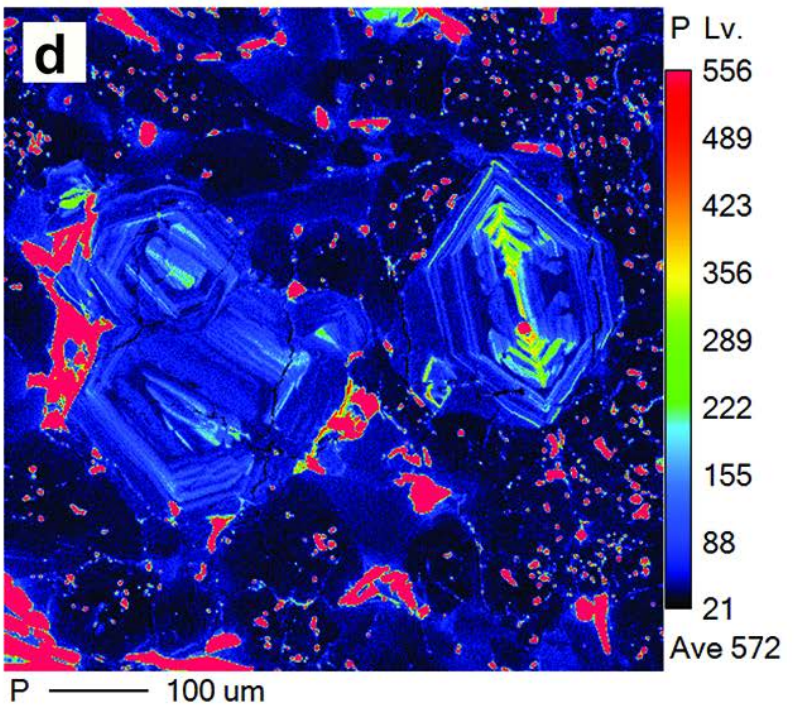
d
P Lv.
556
489
423
356
289
222
155
88
21
Ave 572
P 100 um

FIGURE 1

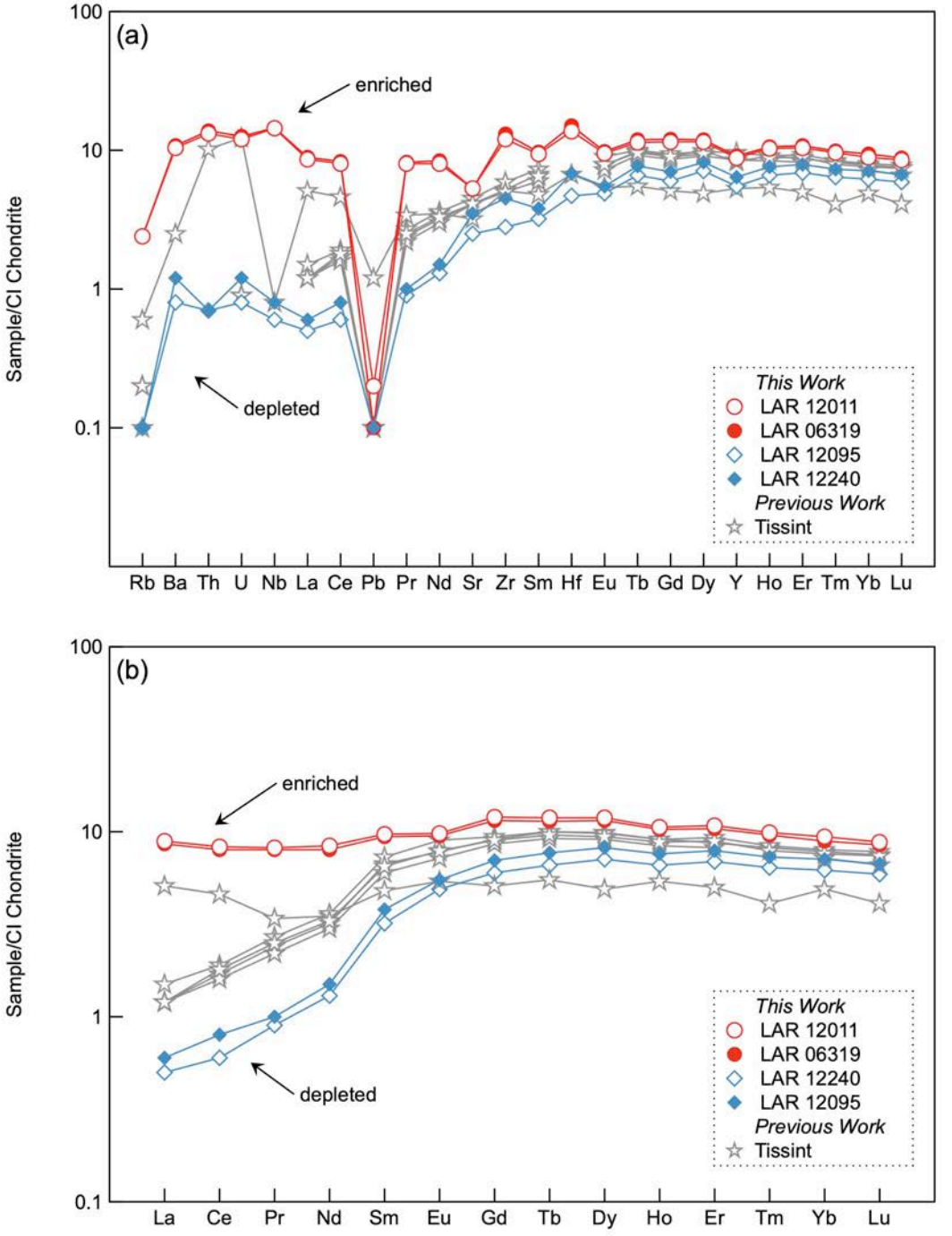
(a)
enriched
depleted
Sample/CI Chondrite
100
10
1
0.1
This Work
LAR 12011
LAR 06319
LAR 12095
LAR 12240
Previous Work
Tissint
Rb Ba Th U Nb La Ce Pb Pr Nd Sr Zr Sm Hf Eu Tb Gd Dy Y Ho Er Tm Yb Lu
(b)
enriched
depleted
Sample/CI Chondrite
100
10
1
0.1
This Work
LAR 12011
LAR 06319
LAR 12240
LAR 12095
Previous Work
Tissint
La Ce Pr Nd Sm Eu Gd Tb Dy Ho Er Tm Yb Lu

FIGURE 2

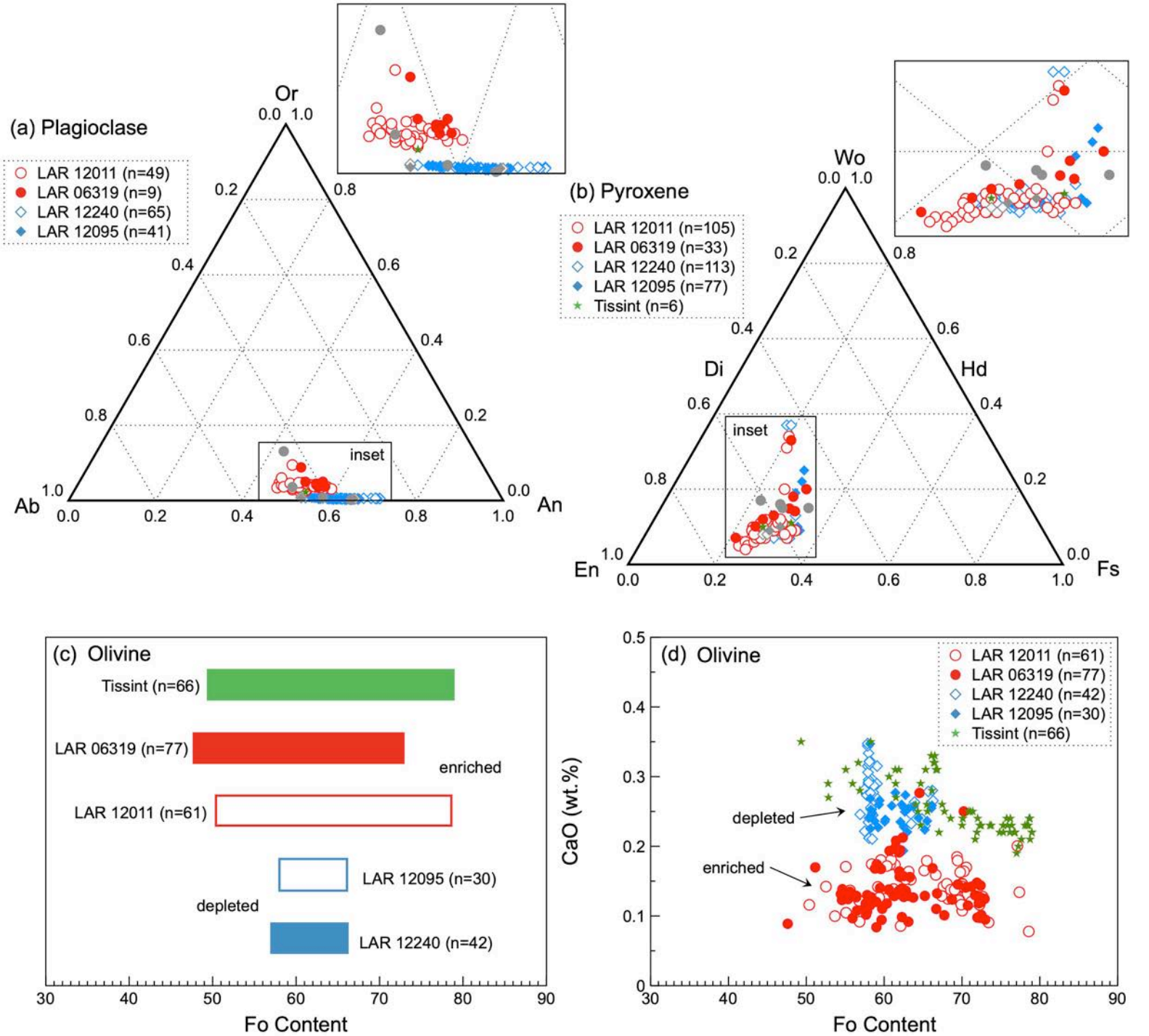
(a) Plagioclase
LAR 12011 (n=49)
LAR 06319 (n=9)
LAR 12240 (n=65)
LAR 12095 (n=41)
Or
Ab
An
inset
(b) Pyroxene
LAR 12011 (n=105)
LAR 06319 (n=33)
LAR 12240 (n=113)
LAR 12095 (n=77)
Tissint (n=6)
Wo
Di
Hd
En
Fs
inset
(c) Olivine
Tissint (n=66)
LAR 06319 (n=77)
enriched
LAR 12011 (n=61)
LAR 12095 (n=30)
depleted
LAR 12240 (n=42)
Fo Content
(d) Olivine
LAR 12011 (n=61)
LAR 06319 (n=77)
LAR 12240 (n=42)
LAR 12095 (n=30)
Tissint (n=66)
depleted
enriched
CaO (wt.%)
Fo Content

FIGURE 3

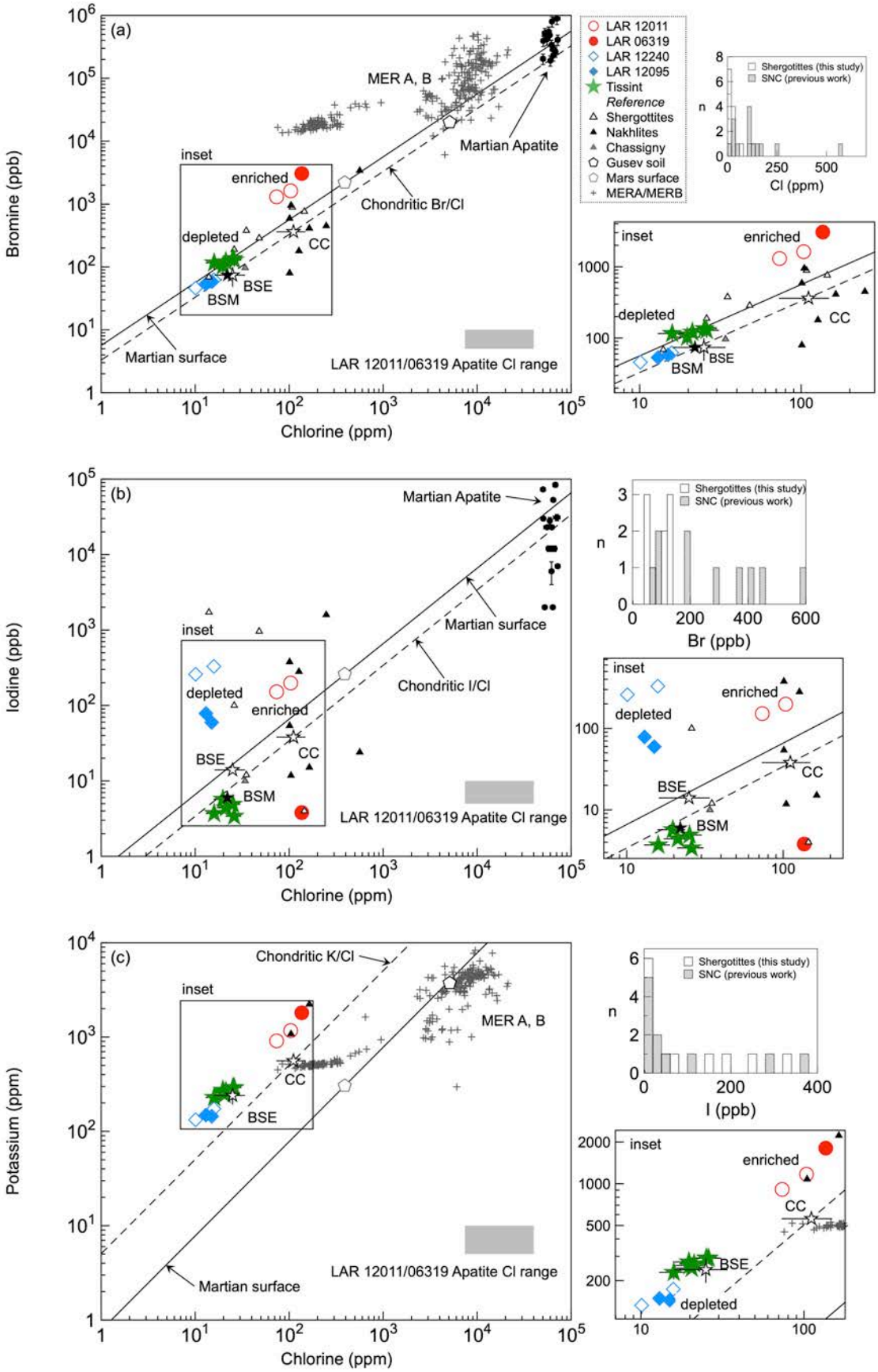
(a)
Bromine (ppb)
Chlorine (ppm)
MER A, B
Martian Apatite
Chondritic Br/Cl
Martian surface
LAR 12011/06319 Apatite Cl range
inset
enriched
depleted
CC
BSE
BSM
LAR 12011
LAR 06319
LAR 12240
LAR 12095
Tissint
Reference
Shergottites
Nakhlites
Chassigny
Gusev soil
Mars surface
MERA/MERB
Shergottites (this study)
SNC (previous work)
n
Cl (ppm)
(b)
Iodine (ppb)
Martian Apatite
Martian surface
Chondritic I/Cl
LAR 12011/06319 Apatite Cl range
Br (ppb)
(c)
Potassium (ppm)
Chondritic K/Cl
MER A, B
Martian surface
LAR 12011/06319 Apatite Cl range
I (ppb)

FIGURE 4

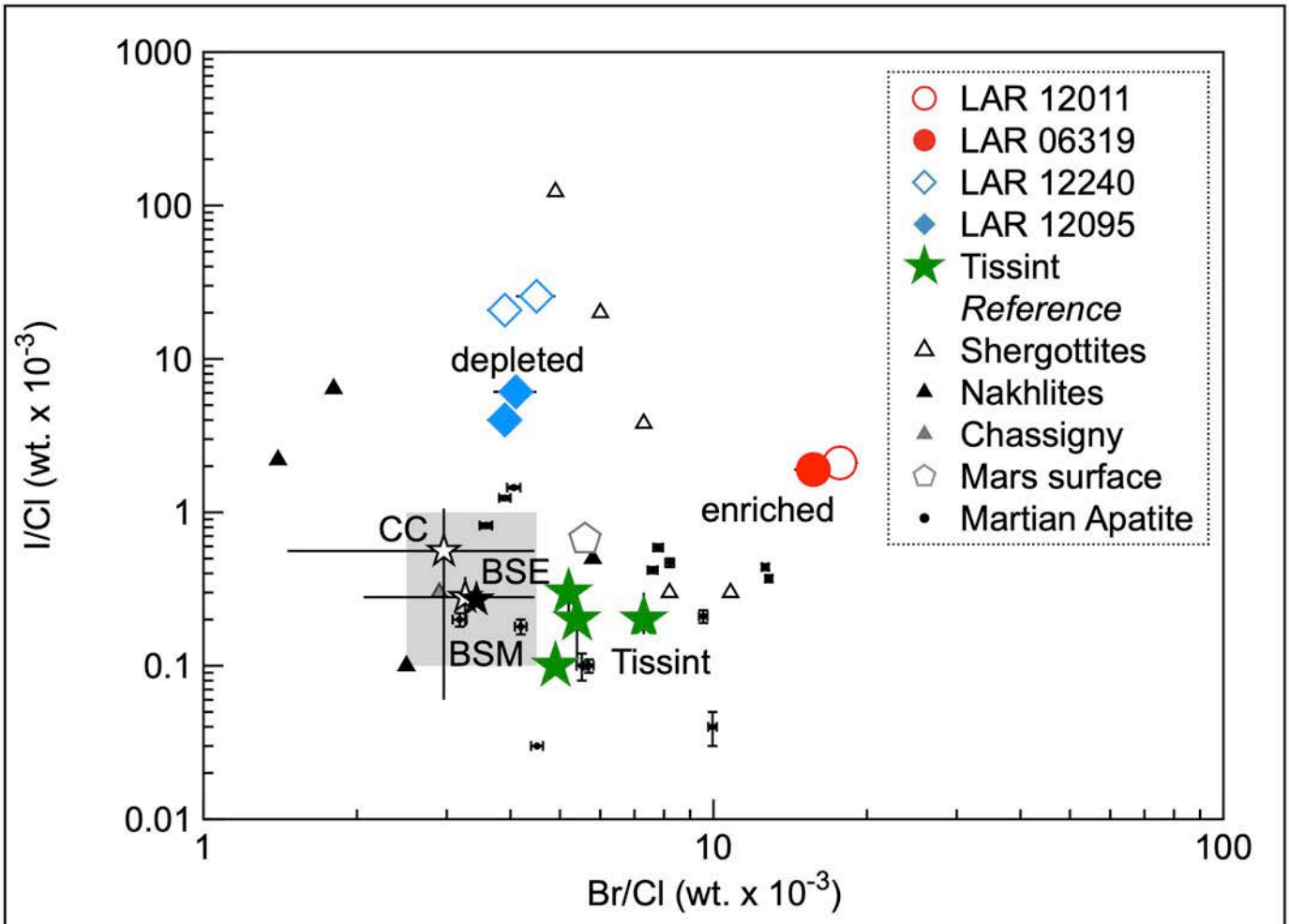
1000
100
10
1
0.1
0.01
I/Cl (wt. x 10-3)
1
10
100
Br/Cl (wt. x 10-3)
LAR 12011
LAR 06319
LAR 12240
LAR 12095
Tissint
Reference
Shergottites
Nakhlites
Chassigny
Mars surface
Martian Apatite
depleted
enriched
CC
BSE
BSM
Tissint

FIGURE 5

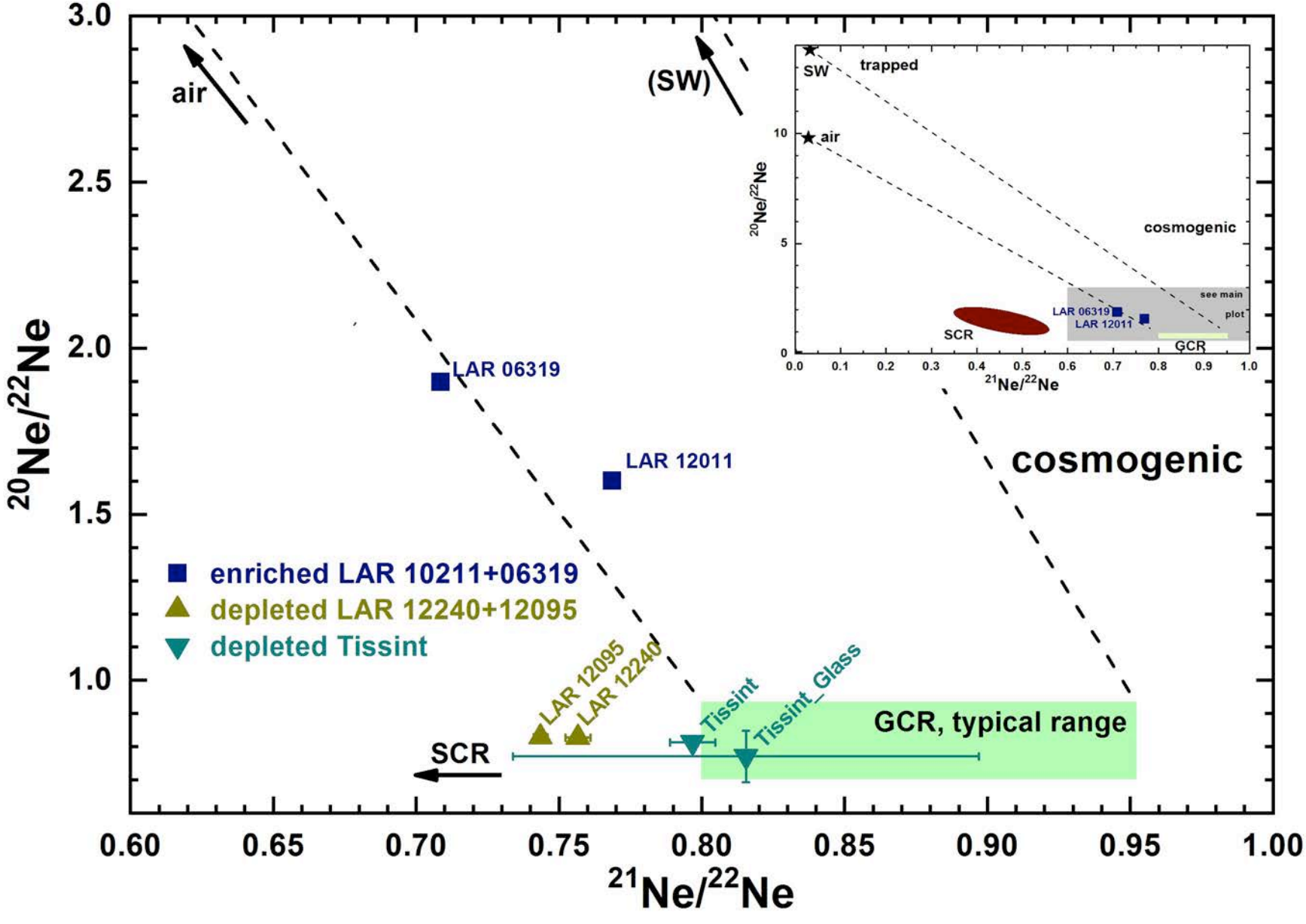
air
(SW)
LAR 06319
LAR 12011
cosmogenic
enriched LAR 10211+06319
depleted LAR 12240+12095
depleted Tissint
LAR 12095
LAR 12240
Tissint
Tissint_Glass
GCR, typical range
SCR
$^{20}Ne/^{22}Ne$
$^{21}Ne/^{22}Ne$
SW
trapped
air
cosmogenic
see main plot
LAR 06319
LAR 12011
SCR
GCR

FIGURE 6

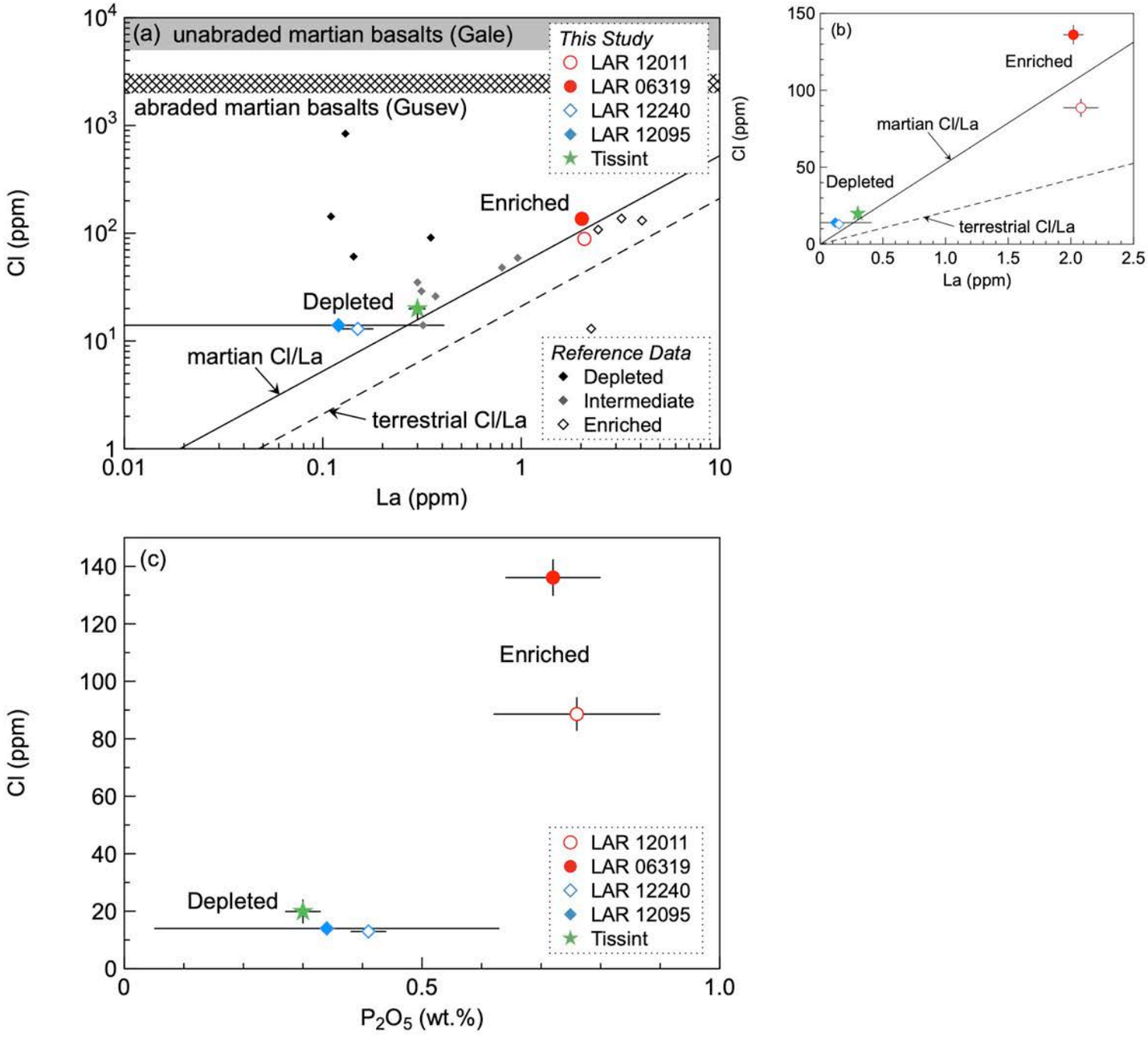
(a) unabraded martian basalts (Gale)
abraded martian basalts (Gusev)
This Study
LAR 12011
LAR 06319
LAR 12240
LAR 12095
Tissint
Enriched
Depleted
martian Cl/La
terrestrial Cl/La
Reference Data
Depleted
Intermediate
Enriched
Cl (ppm)
La (ppm)
(b)
Enriched
martian Cl/La
Depleted
terrestrial Cl/La
La (ppm)
(c)
Enriched
Depleted
LAR 12011
LAR 06319
LAR 12240
LAR 12095
Tissint
Cl (ppm)
P2O5 (wt.%)

FIGURE 7

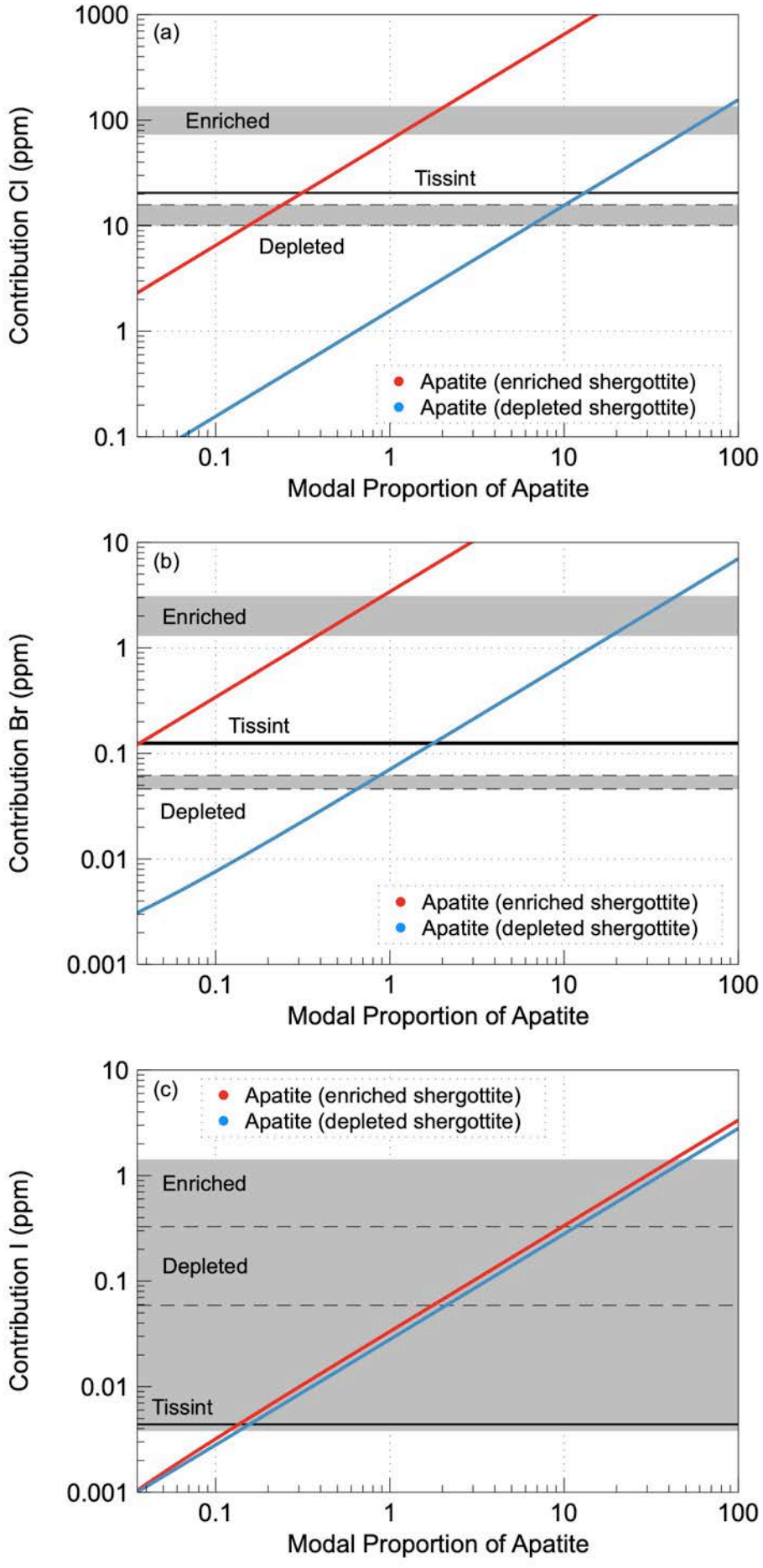
(a)
Enriched
Tissint
Depleted
Apatite (enriched shergottite)
Apatite (depleted shergottite)
Contribution Cl (ppm)
Modal Proportion of Apatite
1000
100
10
1
0.1
0.1
1
10
100
(b)
Enriched
Tissint
Depleted
Apatite (enriched shergottite)
Apatite (depleted shergottite)
Contribution Br (ppm)
Modal Proportion of Apatite
10
1
0.1
0.01
0.001
0.1
1
10
100
(c)
Apatite (enriched shergottite)
Apatite (depleted shergottite)
Enriched
Depleted
Tissint
Contribution I (ppm)
Modal Proportion of Apatite
10
1
0.1
0.01
0.001
0.1
1
10
100

FIGURE 8

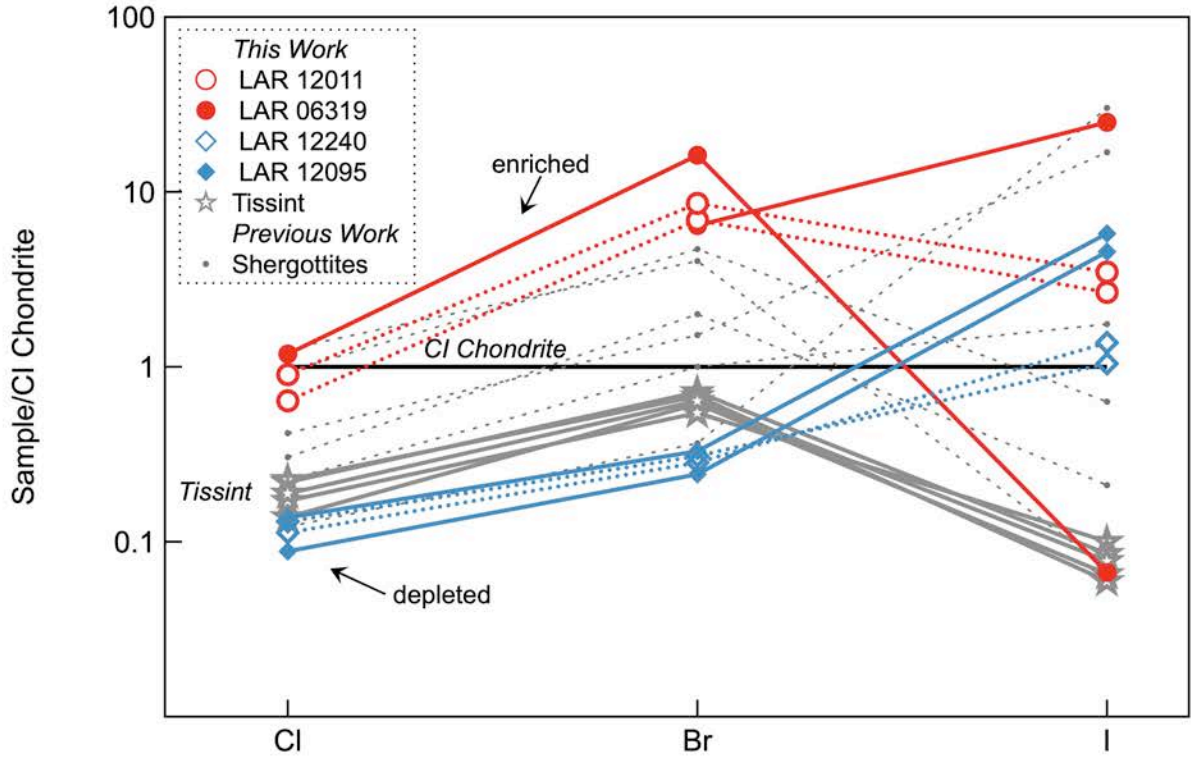
100
10
1
0.1
Sample/CI Chondrite
This Work
LAR 12011
LAR 06319
LAR 12240
LAR 12095
Tissint
Previous Work
Shergottites
enriched
CI Chondrite
Tissint
depleted
Cl
Br
I

FIGURE 9